Eur. Phys. J. C 12, 243–262 (2000)
Digital Object Identifier (DOI) 10.1007/s100529900198

THE EUROPEAN PHYSICAL JOURNAL C

A new global analysis of deep inelastic scattering data

V. Barone[1,2], C. Pascaud[3], F. Zomer[3]

[1] Dipartimento di Fisica Teorica, Università di Torino and INFN, Sezione di Torino, via P. Giuria 1, 10125, Torino, Italy
[2] D.S.T.A., Università A. Avogadro, c.so Borsalino 54, 13100 Alessandria, Italy
[3] Laboratoire de l'Accélérateur Linéaire, IN2P3-CNRS and Université de Paris-Sud, B.P. 34, 91898 Orsay Cedex, France

Received: 16 March 1999 / Published online: 8 December 1999

Abstract. A new QCD analysis of deep inelastic scattering (DIS) data is presented. All available neutrino and antineutrino cross sections are reanalyzed and included in the fit, along with charged-lepton DIS and Drell–Yan data. A massive factorization scheme is used to describe the charm component of the structure functions. Next-to-leading-order parton distribution functions are provided. In particular, the strange-sea density is determined with a higher accuracy with respect to other global fits.

1 Introduction

In deep inelastic scattering (DIS) processes, a neutral or charged lepton l interacts with a nucleon N yielding a lepton l and a set of undetected hadrons X in the final state. The kinematics of this process, $\mathrm{l}(k)+N(p) \to \mathrm{l}'(k')+X$, is determined by two independent variables, besides the energy of the incoming lepton. One usually chooses them among the four Lorentz invariants

$$Q^2 \equiv -q^2 = -(k-k')^2,\ x = \frac{Q^2}{2p\cdot q}\,,$$
$$y = \frac{p\cdot q}{p\cdot k},\ W^2 = (q+p)^2,$$

which are obtained experimentally by measuring the momentum, the direction of the scattered lepton and the initial momenta k, p.

Studies of DIS processes, on both the experimental [1] and theoretical sides [2], have shed light on the nucleon-internal dynamics. In particular, powerful tests of perturbative quantum chromodynamics (pQCD) have been carried out that consist of global analyses performed on a large class of DIS observables. Among these, the structure functions measured in neutrino (antineutrino) DIS play a major role in the determination of the flavor distributions, in particular the valence and the strange-sea densities.

What experiments directly measure is a differential cross section from which the structure functions are extracted by means of a theoretical analysis. This includes the application of electroweak radiative corrections, the determination of $R = \sigma_{\mathrm{L}}/\sigma_{\mathrm{T}}$, the incorporation of possible nuclear effects, etc. In particular, the analysis of neutrino data is a difficult and delicate procedure (see [3] for a clear and detailed description), and so far only a small part of the information accumulated in $\nu(\bar{\nu})$ DIS has been exploited in the QCD parametrizations.

The purpose of this paper is to present a new global analysis of DIS data which includes the available ν and $\bar{\nu}$ cross section measurements[1], in addition to the structure function data collected in charged-lepton DIS experiments. We resort directly to the $\nu(\bar{\nu})$ DIS differential cross sections, avoiding the use of the neutrino structure function results. The latter are the product of a preanalysis which may be (and often is) based on theoretical assumptions different from those of the global fit that one is performing. Thus, for full consistency, we use only *cross section* data. This limits our neutrino (and antineutrino) data set to the BEBC (hydrogen target) [5], CDHS (hydrogen and deuterium targets) [6], and CDHSW (iron target) [7] measurements. The CHARM [8] and CCFR [9] experiments do not provide cross sections but only structure functions; hence their results are not included in our analysis.

The problem with the BEBC, CDHS, and CDHSW data is that they cannot be used in the form in which they were published, since the electroweak radiative corrections were either incomplete or not applied at all and/or the bin center corrections were not performed. Thus we had to reevaluate the neutrino cross sections to take all these corrections into account. This is the preliminary step of our analysis. Since most of the $\nu(\bar{\nu})$ DIS data come from nuclear targets, nuclear corrections must also be applied.

Besides the neutrino data, the structure function measurements from charged-lepton DIS experiments (NMC [10], BCDMS [11], and H1 [12]) are included in our fits. The only non-DIS data we use are the Drell–Yan [13–15] data, which constrain the light sea.

Our fitting procedure is designed in such a way to take properly into account the experimental uncertainties and the correlations among them, which are known to affect

[1] This type of analysis was proposed long ago by M.W. Krasny [4].

the Q^2 slopes of the structure functions and ultimately the determination of the parton densities [16].

An important feature of the QCD analysis presented in this paper is the accurate treatment of the charm contribution to the structure functions. A massive factorization scheme is used, the so-called fixed flavor scheme (FFS) [17]. It is known [18] that for a precise extraction of the strange-sea density, charm mass effects cannot be neglected and have to be correctly incorporated.

In extracting the parton distributions, the neutrino data (in particular, the high-statistics CDHSW data) add a great quantity of information to that coming from charged-lepton DIS. The latter is insufficient to constrain all flavor distributions, being essentially limited to one observable, F_2. Charged-current DIS provides four more independent combinations of parton densities, F_2^ν, $F_2^{\bar\nu}$, xF_3^ν, $xF_3^{\bar\nu}$. As a consequence, the abundance of neutrino data in our fit ensures an excellent accuracy in the determination of the flavor densities.

A special emphasis will be given to the strange-sea density. Because of the lack of data able to constrain it, in the existing fits [19,20], this distribution is tightly related to the nonstrange-sea distributions and is essentially borrowed[2] from the CCFR extraction [22]. Clearly this is not a consistent procedure. Here we present the first fully consistent determination of the strange distribution within a global fit of all parton densities. The wealth of neutrino and antineutrino data will also allow us to test the possible charge asymmetry of the strange sea ($s \neq \bar s$) predicted by some authors.

In the present work, the strong coupling constant is independently fixed to a value close to the world average. In a forthcoming paper we shall study the possibility of determining α_s from the minimization of the total χ^2 of the fit, and discuss the stability of this determination and its correlation with the gluon density.

The article is organized as follows. In Sect. 2, we collect the main theoretical ingredients of the QCD analysis of DIS data. The reevaluation of the neutrino and antineutrino differential cross sections is the content of Sect. 3. The fitting procedure is described in Sect. 4. Finally, the results on cross sections, structure functions, and parton distribution functions are presented in Sect. 5.

2 Deep inelastic scattering in QCD

The differential cross section of neutral-current (NC) DIS of charged leptons (l), in the one-boson approximation and for moderate $Q^2 \ll M_Z^2$, is given by

$$\frac{\mathrm{d}^2\sigma^{\mathrm{lN}}}{\mathrm{d}x\mathrm{d}y} = \frac{8\pi\alpha_{\mathrm{em}}^2 M_{\mathrm{N}} E}{Q^2}\left[xy^2\, F_1^{\mathrm{lN}}(x,Q^2) + \left(1-y-\frac{M_{\mathrm{N}}xy}{2E}\right)F_2^{\mathrm{lN}}(x,Q^2)\right], \quad (1)$$

[2] In the GRV fit, [21] the strange distribution is assumed to be zero at a very low Q^2 scale and then entirely generated by the QCD evolution.

Table 1. Leading-order expressions of F_2 (l: light sector; c: charm sector in the fixed flavor scheme (FFS)). The x and Q^2 arguments have been omitted. Only the slow-rescaled argument ξ has been explicitly indicated

	$F_{2,\mathrm{l}}$	$F_{2,\mathrm{c}}$
$\mathrm{l}^\pm p$	$x[\frac{4}{9}(u+\bar u)+\frac{1}{9}(d+\bar d+s+\bar s)]$	$\frac{4}{9}\,(\frac{\alpha_s}{2\pi})\,C_{2,\mathrm{g}}^{\mathrm{c},(0)}\otimes xg$
$\mathrm{l}^\pm n$	$x[\frac{4}{9}(d+\bar d)+\frac{1}{9}(u+\bar u+s+\bar s)]$	$\frac{4}{9}\,(\frac{\alpha_s}{2\pi})\,C_{2,\mathrm{g}}^{\mathrm{c},(0)}\otimes xg$
νp	$2x[\bar u + d\lvert V_{\mathrm{ud}}\rvert^2 + s\lvert V_{\mathrm{us}}\rvert^2]$	$2\xi[d(\xi)\lvert V_{\mathrm{cd}}\rvert^2 + s(\xi)\lvert V_{\mathrm{cs}}\rvert^2]$
νn	$2x[\bar d + u\lvert V_{\mathrm{ud}}\rvert^2 + s\lvert V_{\mathrm{us}}\rvert^2]$	$2\xi[u(\xi)\lvert V_{\mathrm{cd}}\rvert^2 + s(\xi)\lvert V_{\mathrm{cs}}\rvert^2]$
$\bar\nu p$	$2x[u + \bar d\lvert V_{\mathrm{ud}}\rvert^2 + \bar s\lvert V_{\mathrm{us}}\rvert^2]$	$2\xi[\bar d(\xi)\lvert V_{\mathrm{cd}}\rvert^2 + \bar s(\xi)\lvert V_{\mathrm{cs}}\rvert^2]$
$\bar\nu n$	$2x[d + \bar u\lvert V_{\mathrm{ud}}\rvert^2 + \bar s\lvert V_{\mathrm{us}}\rvert^2]$	$2\xi[\bar u(\xi)\lvert V_{\mathrm{cd}}\rvert^2 + \bar s(\xi)\lvert V_{\mathrm{cs}}\rvert^2]$

If $Q^2 \ll M_Z^2$, charged-lepton NC DIS is essentially an electromagnetic reaction (that is dominated by one-photon exchange), the Z^0 contribution being totally negligible. In (1), $\alpha_{\mathrm{em}} = 1/137$ is the electromagnetic coupling constant, E is the beam energy, and M_{N} is the nucleon mass.

For charged-current (CC) neutrino (antineutrino) DIS, one has

$$\frac{\mathrm{d}^2\sigma^{\nu(\bar\nu)\mathrm{N}}}{\mathrm{d}x\mathrm{d}y} = \frac{G_{\mathrm{F}}^2 M_{\mathrm{N}} E}{\pi}\left(\frac{M_{\mathrm{W}}^2}{Q^2+M_{\mathrm{W}}^2}\right)^2 \times\left[xy^2\, F_1^{\nu(\bar\nu)\mathrm{N}}(x,Q^2) + \left(1-y-\frac{M_{\mathrm{N}}xy}{2E}\right)F_2^{\nu(\bar\nu)\mathrm{N}}(x,Q^2) + (-)\left(y-\frac{y^2}{2}\right)xF_3^{\nu(\bar\nu)\mathrm{N}}(x,Q^2)\right], \quad (2)$$

where M_{W} is the W-boson mass, and G_{F} is the Fermi coupling constant.

In QCD, the structure functions F_2, $F_{\mathrm{L}} = F_2 - 2xF_1$, and xF_3 are given by the convolution of the parton distribution functions (pdf) with some perturbatively calculable coefficient functions. In the kinematic range covered by the analysis presented in this article, the contribution of the b quark is negligible, and the only heavy quark considered is charm. Therefore we split the structure functions into two components

$$F_i(x,Q^2) = F_{i,\mathrm{l}}(x,Q^2) + F_{i,\mathrm{c}}(x,Q^2), \quad i = 2,3,L$$

Table 2. Same as Table 1, for xF_3

	$xF_{3,\mathrm{l}}$	$xF_{3,\mathrm{c}}$
νp	$2x[d\lvert V_{\mathrm{ud}}\rvert^2 + s\lvert V_{\mathrm{us}}\rvert^2 - \bar{u}]$	$2\xi[d(\xi)\lvert V_{\mathrm{cd}}\rvert^2 + s(\xi)\lvert V_{\mathrm{cs}}\rvert^2]$
νn	$2x[u\lvert V_{\mathrm{ud}}\rvert^2 + s\lvert V_{\mathrm{us}}\rvert^2 - \bar{d}]$	$2\xi[u(\xi)\lvert V_{\mathrm{cd}}\rvert^2 + s(\xi)\lvert V_{\mathrm{cs}}\rvert^2]$
$\bar{\nu}p$	$2x[u - \bar{d}\lvert V_{\mathrm{ud}}\rvert^2 - \bar{s}\lvert V_{\mathrm{us}}\rvert^2]$	$-2\xi[\bar{d}(\xi)\lvert V_{\mathrm{cd}}\rvert^2 + \bar{s}(\xi)\lvert V_{\mathrm{cs}}\rvert^2]$
$\bar{\nu}n$	$2x[d - \bar{u}\lvert V_{\mathrm{ud}}\rvert^2 - \bar{s}\lvert V_{\mathrm{us}}\rvert^2]$	$-2\xi[\bar{u}(\xi)\lvert V_{\mathrm{cd}}\rvert^2 + \bar{s}(\xi)\lvert V_{\mathrm{cs}}\rvert^2]$

where $F_{i,\mathrm{l}}(x,Q^2)$ is the light-parton contribution, and $F_{i,\mathrm{c}}(x,Q^2)$ is the charm contribution. In the CC case, the latter mixes charm with light quarks.

The massive scheme that we adopt is the fixed flavor scheme [17] in which charm is a heavy quark in absolute sense of "heavy". This means that there is no such thing as the charm density function, and charm is radiatively produced. Consequently, the number of active flavors is set to 3, irrespective of Q^2. The FFS has been shown to be more stable than the alternative massive scheme, the variable flavor scheme (VFS) [23], at moderate Q^2 where most of the neutrino data lie [24,25].

In the strong coupling, heavy-quark thresholds are accounted for according to the prescription of [26] (with $m_{\mathrm{c}} = 1.5$ GeV and $m_b = 4$ GeV).

The leading-order (LO) expressions for F_2 and xF_3 are collected in Tables 1 and 2. Note that:

- $\xi = x(1 + Q^2/m_{\mathrm{c}}^2)$ is the slow-rescaling variable; $m_{\mathrm{c}} = 1.5$ GeV is the charm mass.
- V_{ij} are the Cabibbo–Kobayashi–Maskawa matrix elements. We shall use $|V_{\mathrm{us}}| = |V_{\mathrm{cd}}| = 0.224$ and $|V_{\mathrm{ud}}| = |V_{\mathrm{cs}}| = \sqrt{1 - |V_{\mathrm{us}}|^2}$.
- The symbol $\otimes$ stands for convolution:

$$f \otimes g = \int_{ax}^{1} \frac{\mathrm{d}z}{z}\, f(z) g(x/z)\,,$$

  where $a = 1$ for the light sector, $a = 1 + 4m_{\mathrm{c}}^2/Q^2$ for NC charm production, and $a = 1 + m_{\mathrm{c}}^2/Q^2$ for CC charm production.
- The LO charm contribution to F_2 in the neutral-current charged-lepton case is an $\mathcal{O}(\alpha_{\mathrm{s}})$ quantity in the fixed flavor scheme. $C_{2,\mathrm{g}}^{\mathrm{c},(0)}$ is the LO Wilson coefficient for the photon–gluon fusion process [27]. Explicitly:

$$F_{2,\mathrm{c}}^{\mathrm{lN}}(x,Q^2) = \frac{4}{9}\,(\frac{\alpha_{\mathrm{s}}}{2\pi})\, C_{2,\mathrm{g}}^{\mathrm{c},(0)}(m_{\mathrm{c}}^2/Q^2) \otimes xg(\mu^2)\,, \quad (3)$$

  where the strong coupling is evaluated at the factorization scale μ, and $C_{2,\mathrm{g}}^{\mathrm{c},(0)}(z, m_{\mathrm{c}}^2/Q^2)$ can be found, for instance, in [17].
- The charm production is different in neutral and charged-current DIS. In the former case, it is given at LO by a gluon splitting into a $\mathrm{c\bar{c}}$ pair. In the latter case, it is given by the direct process $\mathrm{W^+ s} \to \mathrm{c}$, with the slow-rescaling variable taking into account the effect of the charm mass.
- At order α_{s}^0 the longitudinal structure function $F_{\mathrm{L}} = F_2 - 2xF_1$ vanishes.

The QCD analysis performed in this paper is at the next-to-leading-order (NLO) level (the renormalization scheme adopted is $\overline{\mathrm{MS}}$). NLO is $\mathcal{O}(\alpha_{\mathrm{s}})$ for the light sector and the charm contribution to CC DIS, and $\mathcal{O}(\alpha_{\mathrm{s}}^2)$ for the charm contribution to NC DIS in the fixed flavor scheme. Since F_{L} vanishes at order α_{s}^0, we include in our NLO analysis, for consistency with the treatment of the charm structure function, the order-α_{s}^2 contribution to F_{L}, except for the strange-charm component of F_{L}, for which the $\mathcal{O}(\alpha_{\mathrm{s}}^2)$ longitudinal Wilson coefficients are not yet known. This contribution has a very little effect in the kinematic domain of our analysis.

The light-parton components of the structure functions have the form (for illustration, we write only F_2 for the electromagnetic case):

$$F_{2,\mathrm{l}}^{\mathrm{lN}}(x,Q^2) = \sum_{f=\mathrm{q},\bar{\mathrm{q}}} e_f^2 \{(1 + \frac{\alpha_{\mathrm{s}}}{2\pi}\, C_{2,f}^{(1)}) \otimes xf + \frac{\alpha_{\mathrm{s}}}{2\pi}\, C_{2,\mathrm{g}}^{(1)} \otimes xg\}\,. \quad (4)$$

The $\overline{\mathrm{MS}}$ Wilson coefficients $C_{i,\mathrm{q}}^{(1)}$ and $C_{i,\mathrm{g}}^{(1)}$ with $i = 2, 3, L$ can be found in Appendix I of [28]. As mentioned above, for $F_{L,\mathrm{l}}$ we consider also the $\mathcal{O}(\alpha_{\mathrm{s}}^2)$ contributions to the coefficient functions calculated in [29][3].

The parton densities xf and xg are obtained by the solution of the DGLAP equations at NLO [30]. For the light sector, we choose $\sqrt{Q^2}$ as the factorization and renormalization scale.

The NLO expression of the charm contribution to the NC structure functions is

$$\begin{aligned} F_{2,\mathrm{c}}^{\mathrm{lN}}(x,Q^2) = \frac{\alpha_{\mathrm{s}}}{2\pi} \Big\{ & \frac{4}{9} \Big[C_{2,\mathrm{g}}^{\mathrm{c},(0)}(m_{\mathrm{c}}^2/Q^2) \\ & + \frac{\alpha_{\mathrm{s}}}{2\pi}\, C_{2,\mathrm{g}}^{\mathrm{c},(1)}(m_{\mathrm{c}}^2/Q^2) \Big] \otimes xg(\mu^2) \\ & + \frac{\alpha_{\mathrm{s}}^2}{(2\pi)^2} \sum_{f=\mathrm{q},\bar{\mathrm{q}}} \Big[\frac{4}{9}\, C_{2,f}^{\mathrm{c},(1)}(m_{\mathrm{c}}^2/Q^2) \otimes xf(\mu^2) \\ & + e_f^2\, D_{2,f}^{\mathrm{c},(1)}(m_{\mathrm{c}}^2/Q^2) \otimes xf(\mu^2) \Big] \Big\}\,. \end{aligned} \quad (5)$$

The NLO coefficients $C^{\mathrm{c},(1)}$ and $D^{\mathrm{c},(1)}$ for $F_{2,\mathrm{c}}^{\mathrm{lN}}$ and $F_{L,\mathrm{c}}^{\mathrm{lN}}$ have been computed in the fixed flavor scheme in [31]. For our calculations, we have used the tables presented in [32].

The NLO strange-charm component of the structure functions is given by (omitting the Cabibbo-suppressed term and again writing only F_2 for simplicity)

$$F_{2,\mathrm{c}}^{\nu\mathrm{N}}(x,Q^2) = 2\,\{(1 + \frac{\alpha_{\mathrm{s}}}{2\pi} H_{2,f}^{\mathrm{c},(1)}) \otimes \xi s + \frac{\alpha_{\mathrm{s}}}{2\pi} H_{2,\mathrm{g}}^{\mathrm{c},(1)} \otimes \xi g\}\,, \quad (6)$$

[3] We thank W. van Neerven for having provided us the code which computes the order-α_{s}^2 Wilson coefficients of F_{L}.

The Wilson coefficients $H_{i,f}^{\mathrm{c},(1)}$ and $H_{i,\mathrm{g}}^{\mathrm{c},(1)}$ $(i = 2, 3, L)$ have been computed in [33] and can be found, with a convention update, also in [34,35]. The factorization and renormalization scale for the charm structure functions is chosen to be $\sqrt{Q^2 + m_{\mathrm{c}}^2}$.

3 Re-evaluation of neutrino cross sections

3.1 Bin center and radiative corrections

We start with a general description of the procedure of bin center and electroweak radiative corrections. We shall then give the details of the application of this procedure to the various data sets.

The neutrino DIS cross sections are determined experimentally in bins of three kinematic variables, say (x, y, E). The total cross section $\sigma_{ijk}^{\mathrm{tot}}$ corresponding to the bins $[x_i, x_{i+1}]$, $[y_j, y_{j+1}]$, and $[E_k, E_{k+1}]$ is given by

$$\sigma_{ijk}^{\mathrm{tot}} \equiv \int_{x_i}^{x_{i+1}} \int_{y_j}^{y_{j+1}} \int_{E_k}^{E_{k+1}} \frac{\mathrm{d}\phi}{\mathrm{d}E} \frac{\mathrm{d}^2\sigma}{\mathrm{d}x\mathrm{d}y} \,\mathrm{d}E\,\mathrm{d}x\,\mathrm{d}y = \frac{N_{ijk}}{C} \tag{7}$$

where C is the number of scattering centers, N_{ijk} is the number of events corrected for detector effects and background contamination observed in the bin (i, j, k), and $\mathrm{d}\phi/\mathrm{d}E$ is the neutrino beam-energy flux.

In order to relate $\sigma_{ijk}^{\mathrm{tot}}$ to the differential cross section, we invoke the average theorem: There exists at least one point $(\bar{x}_i, \bar{y}_j, \bar{E}_k)$ inside the bin (i, j, k) such that the following relation holds:

$$\frac{\mathrm{d}^2\sigma(\bar{x}_i, \bar{y}_j, \bar{E}_k)}{\mathrm{d}x\mathrm{d}y} = \frac{\sigma_{ijk}^{\mathrm{tot}}}{S_{ijk}}, \tag{8}$$

where $S_{ijk} = \int_{x_i}^{x_{i+1}} \int_{y_j}^{y_{j+1}} \int_{E_k}^{E_{k+1}} \frac{\mathrm{d}\phi}{\mathrm{d}E}\,\mathrm{d}E\,\mathrm{d}x\,\mathrm{d}y$ is the bin surface.

The differential cross section defined in (8) must be corrected for electroweak radiation effects and translated to the bin centers $(x_i^{\mathrm{c}}, y_j^{\mathrm{c}}, E_k^{\mathrm{c}})$. This is done by the construction of an "experimental" Born differential cross section defined as

$$\frac{\mathrm{d}^2\sigma_{\mathrm{exp}}^{\mathrm{B}}(x_i^{\mathrm{c}}, y_j^{\mathrm{c}}, E_k^{\mathrm{c}})}{\mathrm{d}x\mathrm{d}y} \equiv \frac{\mathrm{d}^2\sigma(\bar{x}_i, \bar{y}_j, \bar{E}_k)}{\mathrm{d}x\mathrm{d}y} \times \frac{S_{ijk}\,\mathrm{d}^2\tilde{\sigma}^{\mathrm{B+R}}(x_i^{\mathrm{c}}, y_j^{\mathrm{c}}, E_k^{\mathrm{c}})/\mathrm{d}x\mathrm{d}y}{\int_{x_i}^{x_{i+1}} \int_{y_j}^{y_{j+1}} \int_{E_k}^{E_{k+1}} \frac{\mathrm{d}\phi}{\mathrm{d}E} \frac{\mathrm{d}^2\tilde{\sigma}^{\mathrm{B+R}}}{\mathrm{d}x\mathrm{d}y} \mathrm{d}E\,\mathrm{d}x\,\mathrm{d}y} \times \frac{\mathrm{d}^2\tilde{\sigma}^{\mathrm{B}}(x_i^{\mathrm{c}}, y_j^{\mathrm{c}}, E_k^{\mathrm{c}})/\mathrm{d}x\mathrm{d}y}{\mathrm{d}^2\tilde{\sigma}^{\mathrm{B+R}}(x_i^{\mathrm{c}}, y_j^{\mathrm{c}}, E_k^{\mathrm{c}})/\mathrm{d}x\mathrm{d}y} \tag{9}$$

where the tilde symbol designates the quantities which are theoretically computed, and the superscripts B+R and B mean that these calculations are performed including or not, respectively, the higher-order electroweak corrections. The first term on the r.h.s. of (9) is given by (8). The second term embodies the *bin center corrections* and requires a smooth parametrization of the data. The third term incorporates the *radiative corrections*.

Combining the last two terms, we get

$$\frac{\mathrm{d}\sigma_{\mathrm{exp}}^{\mathrm{B}}(x_i^{\mathrm{c}}, y_j^{\mathrm{c}}, E_k^{\mathrm{c}})}{\mathrm{d}x\mathrm{d}y} \equiv \frac{N_{ijk}}{C} \times \frac{\mathrm{d}\tilde{\sigma}^{\mathrm{B}}(x_i^{\mathrm{c}}, y_j^{\mathrm{c}}, E_k^{\mathrm{c}})/\mathrm{d}x\mathrm{d}y}{\int_{x_i}^{x_{i+1}} \int_{y_j}^{y_{j+1}} \int_{E_k}^{E_{k+1}} \frac{\mathrm{d}\phi}{\mathrm{d}E} \frac{\mathrm{d}\tilde{\sigma}^{\mathrm{B+R}}(x,y,E)}{\mathrm{d}x\mathrm{d}y} \mathrm{d}E\,\mathrm{d}x\,\mathrm{d}y}\,. \tag{10}$$

The electroweak corrections to charged-current DIS were computed in [36,37]. In our analysis we used the program of [38], based on the results of [37]. At the lowest order, radiative corrections include the radiation of virtual and real photons from the charged-lepton and quark legs, and the γ–W box diagram. We found that these corrections can reach $\sim 20\%$ in some kinematic domains. The correction factor – the third term in (9) – is a ratio, hence it is rather insensitive to QCD corrections [3]. Thus, for simplicity, we computed it at leading order in QCD.

We also evaluated the effects of the higher-order γ radiation from the charged-lepton leg [39], using the program HECTOR [40]. This correction typically does not exceed $\sim 0.5\%$, and was applied only to the CDHSW data, which are statistically more significant.

3.1.1 CDHSW corrections

The CDHSW Collaboration published [7] the νFe and $\bar{\nu}$Fe differential cross sections corrected for detector effects and background subtraction. The measurements are binned in x and y for nine different values of the neutrino beam energies E_k^{c} between 23 GeV and 187.6 GeV. Neither the bin center correction in x and y nor the radiative corrections were applied; thus the full correction of (9) is needed.

We cannot use any of the existing fits to evaluate the correction factors of (9) because they do not account for nuclear effects. Thus we adopt an iterative procedure. In the first step, the bin center correction and the radiative corrections are determined independently: the former by a parametrization obtained in two different ways (see below), and the latter by a standard fit (we use the LO-GRV pdf [21]). Then, we perform an LO-QCD fit to the corrected CDHSW cross sections, the CDHS data, and the BCDMS, NMC, and SLAC [41] structure functions[4]. Using the pdf of this fit, we reevaluate the full correction factor of (9) and we iterate this step until the corrected differential cross sections get stable. In practice, to achieve stability, only two iterations are required.

As we have mentioned, the smooth parametrization of the data (required in the bin center correction) is obtained by two different methods: (i) a fit of the CDHSW cross sections (*fitting method*), and (ii) an unfolding procedure (*unfolding method*).

[4] Nuclear corrections to neutrino data are applied as explained in Sect. 3.2.

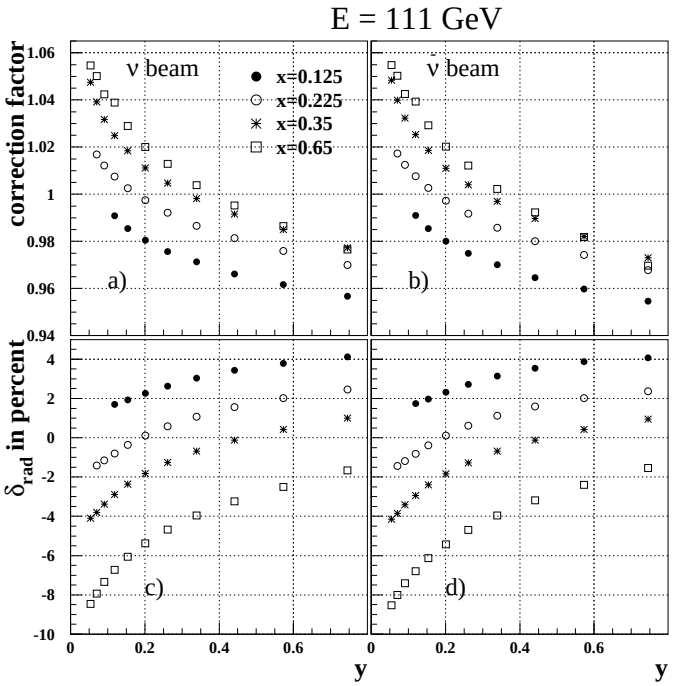

Fig. 1. a Correction factor applied to CDHSW νFe data of the 111 GeV beam-energy sample, as a function of y for various x bins; **b** same as **a** but for CDHSW $\bar{\nu}$Fe data; **c** electroweak radiative correction factor $\delta_{\rm rad} \equiv (\mathrm{d}^2\tilde{\sigma}^{\rm B+R}/\mathrm{d}x\mathrm{d}y)/(\mathrm{d}^2\tilde{\sigma}^{\rm B}/\mathrm{d}x\mathrm{d}y) - 1$ in percent for CDHSW νFe; **d** same as **c** but for CDHSW $\bar{\nu}$Fe

In the first method, the published CDHSW νFe and $\bar{\nu}$Fe differential cross section data are fitted to

$$\int_{x_i}^{x_{i+1}} \int_{y_j}^{y_{j+1}} \frac{\mathrm{d}^2\tilde{\sigma}_{\nu(\bar{\nu})}(x,y,E_k^{\rm c})}{\mathrm{d}x\mathrm{d}y}\mathrm{d}x\mathrm{d}y, \quad k = 1,...,9$$

where $\tilde{\sigma}_{\nu(\bar{\nu})}$ is computed at LO using simple Buras–Gaemers-type pdf [42] (which incorporate analytically the Q^2 dependence). In parallel, we adopted also the unfolding method (described in Appendix A). The difference of the results obtained by the two procedures can be taken as a (partial) estimate of the uncertainty regarding the correction factor applied to neutrino cross sections. We found that after two iterations the results of the two methods are compatible within 1%.

In Fig. 1a,b we show the total correction factors applied to the data of the 111-GeV beam sample, as a function of y_j for fixed x_i. They vary between +6% and −4% and are roughly identical for neutrino and antineutrino beams. In Fig. 1c,d, we show the contribution of the electroweak radiative corrections alone, which turns out to be the dominant one.

As for the normalization of the CDHSW data, in [7] they were normalized by the use of the average total cross sections of [43], i.e., the ratios $\sigma^{\nu\rm Fe}/E_\nu$ ($\sigma^{\bar{\nu}\rm Fe}/E_{\bar{\nu}}$) were assumed to be independent of the beam energy. This is a strong assumption in view of the fact that a linear rise with the energy is not experimentally excluded [43]. It is therefore important to check the energy dependence[5].

Table 3. Results of the minimization of χ^2_ν and $\chi^2_{\bar{\nu}}$. The linear functions of the fits are defined as $\sigma/E = <\sigma/E> (\bar{a}_1 E + \bar{a}_2)$ where $<\sigma/E>$ is the average value (see text). Errors on the parameters are also given

$\bar{a}_1^\nu$	$\bar{a}_2^\nu$	$\bar{a}_1^{\bar{\nu}}$	$\bar{a}_2^{\bar{\nu}}$
$(3 \pm 5) \times 10^{-4}$	0.98 ± 0.05	$(-2.4 \pm 0.5) \times 10^{-5}$	1.00 ± 0.04

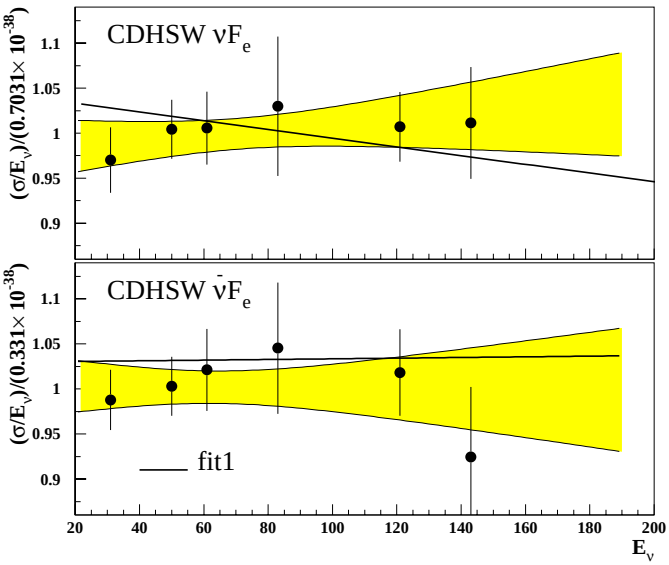

Fig. 2. Total cross sections of νFe (top) and $\bar{\nu}$Fe (bottom) from CDHSW. The shaded areas are the one-standard-deviation error bands corresponding to the linear fits described in Sect. 3.1.1. The curves are the results of `fit1`. The error bars correspond to the quadratic sum of statistical and systematic errors

To this end, we performed a linear fit to the measurements $\sigma^{\nu\rm Fe}(E_\nu)/E_\nu$ and $\sigma^{\bar{\nu}\rm Fe}(E_{\bar{\nu}})/E_{\bar{\nu}}$ of [43]. The results, renormalized by the average values $<\sigma^{\nu\rm Fe}/E_\nu> = 0.703 \times 10^{-38}\mathrm{cm}^2/\mathrm{GeV}$ and $<\sigma^{\bar{\nu}\rm Fe}/E_{\bar{\nu}}> = 0.331 \times 10^{-38}\mathrm{cm}^2/\mathrm{GeV}$, are given in Table 3 and shown in Fig. 2 together with the one-standard-deviation band, which is computed according to the formulas of Appendix B (we call χ^2_ν and $\chi^2_{\bar{\nu}}$ the χ^2 of these fits). A linear rise of $\sigma^{\nu\rm Fe}(E_\nu)/E_\nu$ with E_ν is clearly compatible with the data.

To take into account the effect of the uncertainty of this fit on the CDHSW data, we allow the parameters a_ν and $a_{\bar{\nu}}$ to vary during the global pQCD fit by adding the term

$$\sum_{i,j=1}^{2} (a_i^\nu - \bar{a}_i^\nu) M_{ij}^\nu (a_j^\nu - \bar{a}_j^\nu) + (a_i^{\bar{\nu}} - \bar{a}_i^{\bar{\nu}}) M_{ij}^{\bar{\nu}} (a_j^{\bar{\nu}} - \bar{a}_j^{\bar{\nu}}) \quad (11)$$

[5] We thank M.W. Krasny for having suggested that we take the energy dependence of the CDHSW data into account in our analysis.

to the global χ^2 expression. Here $\bar{a}_i^\nu$ and $\bar{a}_i^{\bar\nu}$ are the parameter values obtained from the preliminary linear fits, and the matrices M_{ij}^ν and $M_{ij}^{\bar\nu}$ are defined as: $M_{ij}^\nu = (1/2)\,\partial^2\chi^2_\nu/\partial a_i^\nu \partial a_j^\nu$, $M_{ij}^{\bar\nu} = (1/2)\,\partial^2\chi^2_{\bar\nu}/\partial a_i^{\bar\nu}\partial a_j^{\bar\nu}$.

Another work done on the CDHSW data involves the separation of correlated and uncorrelated systematic errors. The correlated systematic errors are dominated [44] by a possible shift of the hadronic energy by ± 0.5 GeV. Because no information has been published, we had to estimate the effects of this uncertainty on the cross section measurements. In CDHSW, the beam energy E_ν ($E_{\bar\nu}$) is experimentally reconstructed [7] via $E_\nu = E_\mu + E_X - M_\mathrm{N}$, where E_μ is the measured outgoing muon energy and E_X is the measured hadronic energy in the final state. Thus a shift of the hadronic energy induces a variation of the kinematic variables: $(x, y, Q^2) \to (x_\pm, y_\pm, Q^2_\pm)$. Our estimate of the relative differential cross section error $\delta^\pm_{ijk}$ induced by such shifts is therefore

$$\delta^\pm_{ijk} = \frac{\int_{x_i}^{x_{i+1}}\int_{y_j}^{y_{j+1}} \frac{\mathrm{d}^2\tilde\sigma^{\mathrm{B+R}}(x^\pm, y^\pm, E_k^\pm)}{\mathrm{d}x\mathrm{d}y}\mathrm{d}x\mathrm{d}y}{\int_{x_i}^{x_{i+1}}\int_{y_j}^{y_{j+1}} \frac{\mathrm{d}^2\tilde\sigma^{\mathrm{B+R}}(x,y,E)}{\mathrm{d}x\mathrm{d}y}\mathrm{d}x\mathrm{d}y}$$

where the cross sections $\sigma^{\mathrm{B+R}}$ are computed as described above. The uncorrelated systematic errors are then obtained by the quadratic subtraction of the estimated correlated errors from the published systematic errors $\sigma^{\mathrm{syst}}_{ijk}$

$$\sigma^{\mathrm{uncor}}_{ijk} = \sqrt{(\sigma^{\mathrm{syst}}_{ijk})^2 - \max(\delta^+_{ijk}, \delta^-_{ijk})^2}.$$

The treatment of both types of errors in the fit is described in Sect. 4.

Finally, because CDHSW belongs to an old generation of experiments, one may worry that possible sources of errors at high y have been neglected in their analysis. In particular, one may question two points of the CDHSW analysis (see [3] for more details): (i) a rejection cut against the dimuon events was used, but no correction for it was applied; (ii) the background coming from muon production in hadronic showers was not taken into account. Using the recent CCFR results on $\sigma^{\nu,\bar\nu}_{2\mu}/\sigma^{\nu,\bar\nu}_{1\mu}$ [45] and on the production rate of muons in hadronic showers [46], we estimated the effect of these two sources of errors on the measurements and found it to be at the level of 1% at most.

3.1.2 CDHS corrections

The CDHS Collaboration measured [6] the $\nu(\bar\nu)$H and $\nu(\bar\nu)$Fe differential cross sections. Both the bin center corrections and the radiative corrections were applied. The latter, however, are incomplete. Only the γ radiation from the muon leg was in fact considered. Hence, our first step was to uncorrect the published CDHS cross sections as follows:

$$\frac{\mathrm{d}^2\sigma_{\mathrm{uncorr}}(x_i^\mathrm{c}, y_j^\mathrm{c}, E_k^\mathrm{c})}{\mathrm{d}x\mathrm{d}y} = \frac{\mathrm{d}^2\sigma_{\mathrm{publ}}(x_i^\mathrm{c}, y_j^\mathrm{c}, E_k^\mathrm{c})}{\mathrm{d}x\mathrm{d}y} \times \frac{\mathrm{d}^2\tilde\sigma^{\mathrm{B}+\mu}(x_i^\mathrm{c}, y_j^\mathrm{c}, E_k^\mathrm{c})/\mathrm{d}x\mathrm{d}y}{\mathrm{d}^2\tilde\sigma^{\mathrm{B}}(x_i^\mathrm{c}, y_j^\mathrm{c}, E_k^\mathrm{c})/\mathrm{d}x\mathrm{d}y}\,, \quad (12)$$

where the superscript $\mathrm{B}+\mu$ means that only the radiation from the muon leg was included (to compute it, we used a modified leading-order version of the HECTOR program).

Then we applied to $\mathrm{d}^2\sigma_{\mathrm{uncorr}}/\mathrm{d}x\,\mathrm{d}y$ the full radiative correction factor (i.e., the third term in (9)

$$\frac{\mathrm{d}^2\sigma^{\mathrm{B}}_{\mathrm{exp}}(x_i^\mathrm{c}, y_j^\mathrm{c}, E_k^\mathrm{c})}{\mathrm{d}x\mathrm{d}y} = \frac{\mathrm{d}^2\sigma_{\mathrm{uncorr}}(x_i^\mathrm{c}, y_j^\mathrm{c}, E_k^\mathrm{c})}{\mathrm{d}x\mathrm{d}y} \times \frac{\mathrm{d}^2\tilde\sigma^{\mathrm{B}}(x_i^\mathrm{c}, y_j^\mathrm{c}, E_k^\mathrm{c})/\mathrm{d}x\mathrm{d}y}{\mathrm{d}^2\tilde\sigma^{\mathrm{B+R}}(x_i^\mathrm{c}, y_j^\mathrm{c}, E_k^\mathrm{c})/\mathrm{d}x\mathrm{d}y}\,. \quad (13)$$

In the original paper [6], iron and hydrogen data were normalized by the use of $\sigma^{\nu\mathrm{Fe}}/E_\nu = 0.625\times10^{-38}\mathrm{cm}^2/\mathrm{GeV}$ and $\sigma^{\bar\nu\mathrm{Fe}}/E_{\bar\nu} = 0.3\times10^{-38}\mathrm{cm}^2/\mathrm{GeV}$. Since that time, the total νFe and $\bar\nu$Fe cross sections have been measured more precisely [43]. We therefore applied a new overall correction factor corresponding to $\sigma^{\nu\mathrm{Fe}}/E_\nu = 0.703\times10^{-38}\mathrm{cm}^2/\mathrm{GeV}$ and $\sigma^{\bar\nu\mathrm{Fe}}/E_{\bar\nu} = 0.331\times10^{-38}\mathrm{cm}^2/\mathrm{GeV}$ [43]. We have also improved the overall normalization of the hydrogen data, combining the CDHS [6] $\sigma^{\nu(\bar\nu)\mathrm{H}}/\sigma^{\nu(\bar\nu)\mathrm{Fe}}$ and BEBC [47] $\sigma^{\nu(\bar\nu)\mathrm{H}}/\sigma^{\nu(\bar\nu)Ne}$ results. Assuming no correlations between these experiments, we determined the absolute normalization of the CDHS hydrogen data using: $\sigma^{\nu\mathrm{H}}/E_\nu = 0.451\times10^{-38}\mathrm{cm}^2/\mathrm{GeV}$ and $\sigma^{\bar\nu\mathrm{H}}/E_{\bar\nu} = 0.473\times10^{-38}\mathrm{cm}^2/\mathrm{GeV}$. The remaining error is 3.3% for the neutrino beam and 5.3% for the antineutrino beam. In summary, the νFe, $\bar\nu$Fe, νH and $\bar\nu$H published CDHS data have been renormalized by +12.5%, +10.3%, +14.5% and +20.6%, respectively.

3.1.3 BEBC measurements

Among the BEBC publications, only one [5] gives enough information for the differential cross sections to be reconstructed without any QCD assumptions. In this article, the corrected number of events is given in bins of x and y for a given range of Q^2. As in the case of the CDHS data, the radiative corrections were applied incompletely, considering only the radiation from the muon leg. Hence we uncorrected the published BEBC data as we did for CDHS (except that now we have the *number of events* instead of the *differential cross sections*)

$$N^{\mathrm{uncorr}}_{ijk} = N^{\mathrm{publ}}_{ijk} \times \frac{\int_{x_i}^{x_{i+1}}\int_{y_j}^{y_{j+1}}\int_{E_{\min}}^{E_{\max}} \frac{\mathrm{d}\phi}{\mathrm{d}E}\frac{\mathrm{d}^2\tilde\sigma^{\mathrm{B}+\mu}(x,y,E)}{\mathrm{d}x\mathrm{d}y}\mathrm{d}x\mathrm{d}y\mathrm{d}E}{\int_{x_i}^{x_{i+1}}\int_{y_j}^{y_{j+1}}\int_{E_{\min}}^{E_{\max}} \frac{\mathrm{d}\phi}{\mathrm{d}E}\frac{\mathrm{d}^2\tilde\sigma^{\mathrm{B}}(x,y,E)}{\mathrm{d}x\mathrm{d}y}\mathrm{d}x\mathrm{d}y\mathrm{d}E}\,. \quad (14)$$

Then we inserted $N^{\mathrm{uncorr}}_{ijk}$ into (10) and constructed the experimental Born cross section

$$\frac{\mathrm{d}^2\sigma^{\mathrm{B}}_{\mathrm{exp}}(x_i^\mathrm{c}, y_j^\mathrm{c}, E_k^\mathrm{c})}{\mathrm{d}x\mathrm{d}y} = \frac{N^{\mathrm{uncorr}}_{ijk}}{C} \times \frac{\mathrm{d}\tilde\sigma^{\mathrm{B}}(x_i^\mathrm{c}, y_j^\mathrm{c}, E_k^\mathrm{c})/\mathrm{d}x\mathrm{d}y}{\int_{x_i}^{x_{i+1}}\int_{y_j}^{y_{j+1}}\int_{E_{\min}}^{E_{\max}} \frac{\mathrm{d}\phi}{\mathrm{d}E}\frac{\mathrm{d}\tilde\sigma^{\mathrm{B+R}}(x,y,E)}{\mathrm{d}x\mathrm{d}y}\mathrm{d}E\,\mathrm{d}x\,\mathrm{d}y}\,. \quad (15)$$

The beam-energy flux function of [48] was used to compute the correction factors[6], with the kinematic cuts applied in the data analysis taken into account: $Q^2 > 2$ GeV^2, $W^2 > 4$ GeV^2, $5 < E < 160$ GeV and $E_\mu > 5$ GeV (E_μ being the scattered muon energy).

One should notice that: (i) The beam-energy flux is not known absolutely, hence the absolute normalization of the data has to be determined by the global fit. (ii) The systematic errors are not available.

3.2 Nuclear effects

Most of the neutrino DIS data come from experiments with nuclear targets (deuteron or heavy nuclei). Thus they have to be corrected for nuclear effects, which are known to be quite relevant (see, for instance, [49,50]).

3.2.1 Deuteron

We correct the calculated nucleon structure functions for nuclear binding, Fermi motion, and off-shell effects using the results of the covariant approach of Melnitchouk, et al. [51][7]. The neutrino structure functions $F_1^{\nu\mathrm{D}}$, $F_2^{\nu\mathrm{D}}$ and $F_3^{\nu\mathrm{D}}$ are treated analogously.

The calculation of [51] describes only the high-x ($x \gtrsim 0.2$) behavior of the deuteron structure functions. At small x, other mechanisms are at work (antishadowing and shadowing), but they are negligible in the x and Q^2 regions of the deuteron data entering our analysis [52].

3.2.2 Heavy nuclei

All CDHSW and a large fraction of CDHS data are obtained from scattering off iron nuclei. Since the theoretical understanding of nuclear effects in heavy nuclei is still uncertain and model-dependent [49,50], we adopt an empirical procedure to perform the nuclear corrections.

The experimental $\nu(\bar\nu)$Fe differential cross sections are fitted to

$$\mathrm{d}\sigma^{\nu(\bar\nu)\mathrm{Fe}} = \frac{\mathrm{d}\sigma_{\mathrm{iso}}^{\nu(\bar\nu)\mathrm{Fe}}}{R_{\mathrm{iso}}^{\nu(\bar\nu)}} \,, \tag{16}$$

where $R_{\mathrm{iso}}^{\nu(\bar\nu)}$ is the correction factor for the nonisoscalarity of iron,

$$R_{\mathrm{iso}}^{\nu(\bar\nu)} = \frac{(\mathrm{d}\sigma^{\nu(\bar\nu)\mathrm{p}} + \mathrm{d}\sigma^{\nu(\bar\nu)n})/2}{(Z\,\mathrm{d}\sigma^{\nu(\bar\nu)\mathrm{p}} + (A-Z)\,\mathrm{d}\sigma^{\nu(\bar\nu)n})/A} \quad (A = 55.8,\ Z = 26) \,, \tag{17}$$

and $\mathrm{d}\sigma_{\mathrm{iso}}^{\nu(\bar\nu)\mathrm{Fe}}$ is the isoscalar iron cross section which incorporates the nuclear corrections. Thus

$$\mathrm{d}\sigma_{\mathrm{iso}}^{\nu(\bar\nu)\mathrm{Fe}} = \mathrm{d}\sigma^{\nu(\bar\nu)\mathrm{D}} \times R_{\mathrm{nucl}}^{\mathrm{iso}}$$

where $R_{\mathrm{nucl}}^{\mathrm{iso}}$ is a function embodying the nuclear effects on an isoscalar target. $R_{\mathrm{nucl}}^{\mathrm{iso}}$ consists of two factors

$$R_{\mathrm{nucl}}^{\mathrm{iso}} = R_{\mathrm{Fe/D}} \times R_{\mathrm{iso}}^{\mathrm{l}} \,. \tag{18}$$

The first factor is the Fe/D structure function ratio

$$R_{\mathrm{Fe/D}} = \frac{F_2^{\mathrm{Fe}}}{F_2^{\mathrm{D}}} \,, \tag{19}$$

which is obtained from a fit to the published experimental data on $F_2^{\mathrm{Fe}}/F_2^{\mathrm{D}}$, uncorrected for isoscalarity. The second factor contains the isoscalarity corrections

$$R_{\mathrm{iso}}^{\mathrm{l}} = \frac{(F_2^{\mathrm{lp}} + F_2^{\mathrm{ln}})/2}{(Z\,F_2^{\mathrm{lp}} + (A-Z)\,F_2^{\mathrm{ln}})/A} \,. \tag{20}$$

$R_{\mathrm{Fe/D}}$ is a function of x only because there is no experimental evidence of a significant Q^2 dependence (for a recent study, see [53]). Theoretically, a higher-twist (i.e., power-like) Q^2 dependence is expected at small x and $Q^2 \sim 1$ GeV^2 [54,55], but at larger Q^2, in the region covered by our analysis, shadowing is a scaling phenomenon [56,57].

The small-x ($x < 0.1$) νFe and $\bar\nu$Fe are excluded in our analysis. The reason is that in this region, there are a number of uncertainty sources affecting the determination of R_{nucl}. First of all, there is an unsolved discrepancy between the two measurements $R_{\mathrm{Fe/D}}$ at small x, namely between E665 [58] and NMC [53]. Second, the use of the *charged-lepton* DIS data to determine the Fe/D ratio of *neutrino* cross sections in (16) is justified by the BEBC Ne target results' [59] being in good agreement with the NMC results on C [53] (see [1]), but the situation is experimentally not so clear for $x \lesssim 0.1$, where different nuclear corrections for charged-lepton and neutrino structure functions are expected from a theoretical point of view [60]. Finally, the F_2 and xF_3 corrections might be different at small x [61]. Thus the cut at $x = 0.1$ removes from our fits the more controversial kinematic region, as it does for nuclear corrections.

We then performed a fit to the SLAC [62] BCDMS [63] $F_2^{\mu\mathrm{Fe}}/F_2^{\mu\mathrm{D}}$ data in the range $0.1 < x < 0.65$. For the function $R_{\mathrm{Fe/D}}(x)$, we chose the empirical form

$$R_{\mathrm{Fe/D}}(x) = \alpha_1 + \alpha_2 x + \alpha_3 x^2 \tag{21}$$

where α_i, $i = 1,2,3$ are the free parameters of the fit. The parameters $\bar\alpha_i$ minimizing the χ^2 of this fit (we shall denote it $\chi^2_{\mathrm{Fe/D}}$) are given in Table 4. The result of the fit is shown in Fig. 3 together with the one-standard-deviation error band.

In Fig. 4a,b, we plotted the isoscalarity and nuclear +isoscalarity corrections computed from the structure functions obtained with our fit (see Sect. 5).

4 The analysis

4.1 Data entering the fit

Our analysis includes the neutrino and antineutrino cross section data of BEBC [5], CDHS [6], and CDHSW [7]. The

[6] We thank U. Katz for having provided us the FORTRAN code computing the beam-energy fluxes used in [48].

[7] We thank W. Melnitchouk for having provided us the computer code of his calculation.

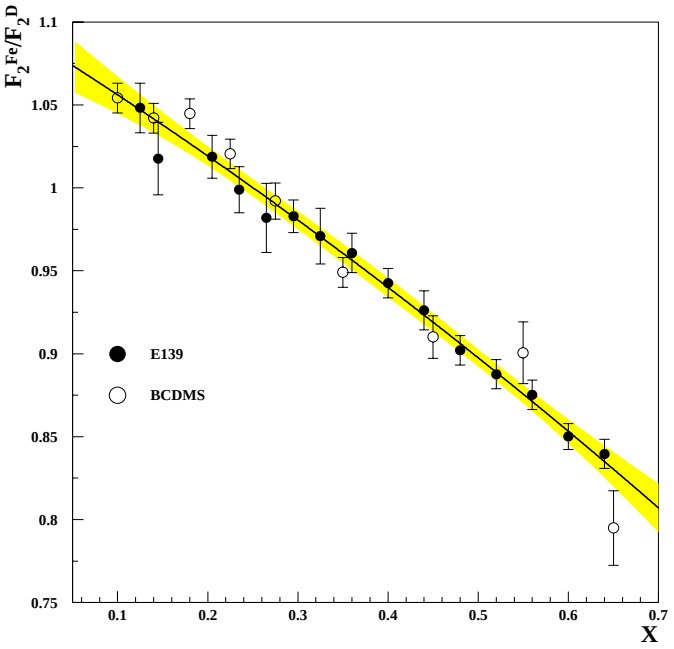

Fig. 3. Fe/D structure function ratio. The full line is the result of a second-order polynomial fit, and the shaded area is the corresponding one-standard-deviation error band (see Sect. 3.2). The error bars correspond to the quadratic sum of statistical and systematic errors

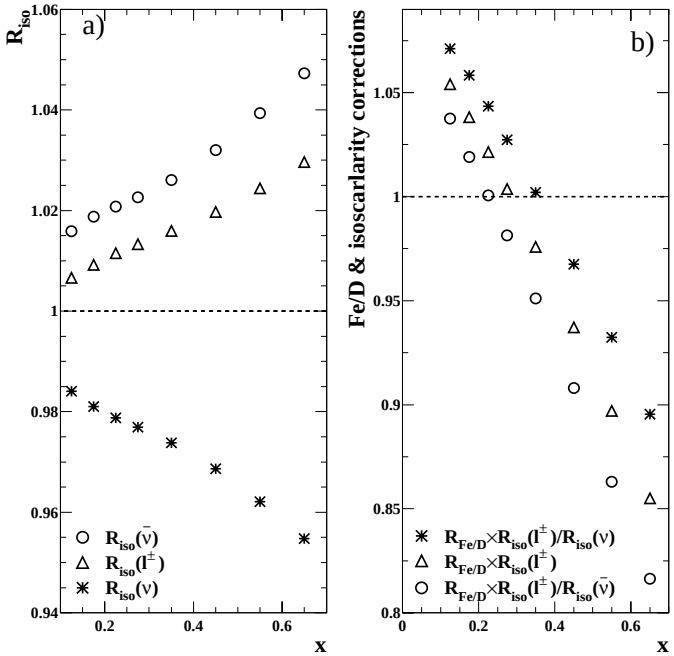

Fig. 4a,b. Corrections applied to iron target data: **a** isoscalarity corrections; **b** nuclear and isoscalarity corrections

Table 4. Results of the minimization of $\chi^2_{\mathrm{Fe/D}}$ (see text)

$\bar{\alpha}_1$	$\bar{\alpha}_2$	$\bar{\alpha}_3$
1.091 ± 0.021	-0.34 ± 0.12	-0.09 ± 0.16

Table 5. Number of events and the limits of the kinematic domain covered by the neutrino experiments considered in our analysis

	events	Δx	ΔQ^2 (GeV^2)	Δy
CDHSW (νFe)	640 000	0.015–0.65	0.2–240	0.037–0.87
CDHSW ($\bar{\nu}$Fe)	550 000	”	”	”
CDHS (νH)	2 100	”	”	”
CDHS ($\bar{\nu}$H)	1 100	”	”	”
BEBC (νD)	12 100	0.03–0.65	3–75	0.05–0.95
BEBC ($\bar{\nu}$D)	5 400	”	”	”
BEBC (νH)	9 800	0.03–0.65	3–75	0.05–0.95
BEBC ($\bar{\nu}$H)	4 900	”	”	”

Table 6. Kinematic range of the charged-lepton DIS and Drell–Yan (DY) data sets entering our fits

	Δx	ΔQ^2 (GeV^2)
NMC (μp, μD)	0.008–0.5	0.8–60
BCDMS (μp)	0.07–0.75	7.5–230
H1-94 (ep)	3.2×10^{-5}–0.32	1.5–5000
E605 (DY)	0.12–0.4	22.6–248
NA51 (DY)	0.18	27.2
E866 (DY)	0.036–0.312	30–164

number of collected events, the number of points, and the kinematic domain covered by these experiments are listed in Table 5.

Besides the neutrino data, which we discussed at length in Sect. 3, the bulk of data entering our fits consist of structure functions from various charged-lepton DIS experiments: BCDMS [11], H1 [12], and NMC [10] (see Table 6).

As for BCDMS, we do not use the merged structure function data, which is obtained by measurements put together at different beam energies, but rather the data on the reduced cross section

$$\frac{Q^2}{4\pi\alpha_{\mathrm{em}}^2 M_{\mathrm{N}} E}\,\frac{1}{Y}\,\frac{\mathrm{d}^2\sigma}{\mathrm{d}x\mathrm{d}y}\,, \qquad Y=1+(1-y)^2-\frac{M_{\mathrm{N}}xy}{E}\,, \quad (22)$$

for each beam energy (we retrieved the original data from [64]).

So that a redundancy of data sets can be avoided, and (most importantly) the number of experimental parameters in the χ^2 minimization limited, the CDHS iron data, which are in agreement with the CDHSW data, do not enter the fit. For the same reasons, the ZEUS F_2 data [65] are not included (ZEUS and H1 1994 data are consistent within 1–2%, as shown by a recent pQCD analysis [66]).

Drell–Yan (DY) data are introduced to constrain the nonstrange sea. Three measurements are used. We fitted the differential cross section for the reaction pCu$\to \mu^+\mu^- X$ measured by E605 [13]. The cross section is calculated at NLO[8]. For Drell–Yan processes, the charm contribution is small [68] and is neglected in our analysis. No higher-twist corrections are required [69] since the kinematic domain covered by E605 avoids the phase space boundaries where these corrections are expected to be important[9].

The other Drell–Yan results that we use are the measurements of the DY asymmetry in pp and pD collisions by NA51 [14] and E866 [15]. These data constrain the ratio $\bar{u}/\bar{d}$.

The kinematic cuts applied to the DIS data entering the fit are:

– $Q^2 \geq 3.5$ GeV^2 and $W^2 \geq 10$ GeV^2.

In this region, higher-twist effects are negligible [71]. Target mass corrections [72] are also very small but have been taken into account in our calculations.

Because of the W^2 and Q^2 cuts, the E665 [73], H1 (1995) [74], SLAC [41], and ZEUS (1995) F_2 data [75] do not enter our fits.

Finally, we reject the CDHSW data with $x < 0.1$. The reason for this cut is threefold: (i) the systematic errors in the low-x region are large [44]; (ii) the nuclear corrections at small x are not completely under control, as was discussed in Sect. 3.2; (iii) at low x, the CDHSW results disagree with the CCFR findings for the cross sections [76] and for the structure functions [3].

4.2 Fitting procedure

The main steps of our fitting procedure are summarized below. For each iteration:

1. The pdf are parametrized at a given value of the momentum transfer, denoted Q_0. We choose $Q_0^2 = 4$ GeV^2.
2. The DGLAP equations are solved numerically in the x space [77] (see [78] for a comparison of different NLO evolution codes).
3. The evolved pdf are convoluted with the Wilson coefficients to obtain the structure functions (see Sect. 2).
4. Assuming that all experimental uncertainties are normally distributed the χ^2 is computed as

$$\chi^2 = \sum_{exp}\sum_{dat} \frac{[\mathcal{O}^{dat}_{exp} - \mathcal{O}^{\rm fit} \times (1 - \nu_{exp}\sigma_{exp} - \sum_k \delta^{dat}_k(s^{exp}_k))]^2}{\sigma^2_{dat,\rm stat} + \sigma^2_{dat,\rm uncor}} + \sum_{exp}\nu^2_{exp} + \sum_{exp}\sum_k (s^{exp}_k)^2 + \sum_{i,j=1}^{2}[(a^\nu_i - \bar{a}^\nu_i)M^\nu_{ij}(a^\nu_j - \bar{a}^\nu_j) + (a^{\bar\nu}_i - \bar{a}^{\bar\nu}_i)M^{\bar\nu}_{ij}(a^{\bar\nu}_j - \bar{a}^{\bar\nu}_j)], \quad (23)$$

where $\mathcal{O}$ stands for the observables (structure functions and differential cross sections). The first two sums run over the data (*dat*) of the various experiments (*exp*); σ_{exp} is the relative overall normalization uncertainty; $\sigma_{dat,\rm stat}$ and $\sigma_{dat,\rm uncor}$ are the statistical error and the uncorrelated systematic error, respectively, corresponding to the datum *dat*; ν_{exp} is the number of standard deviations corresponding to the overall normalization of the experimental sample *exp*. $\delta^{dat}_k(s^{exp}_k)$ is the relative shift of the datum *dat* induced by a change by s^{exp}_k standard deviations of the k^{th} correlated systematic uncertainty source of the experiment *exp*; it is estimated by

$$\delta^{dat}_k(s^{exp}_k) = \frac{\mathcal{O}^{dat}_{exp}(s^{exp}_k = +1) - \mathcal{O}^{dat}_{exp}(s^{exp}_k = -1)}{2\mathcal{O}^{dat}_{exp}}\, s^{exp}_k + \left[\frac{\mathcal{O}^{dat}_{exp}(s^{exp}_k = +1) + \mathcal{O}^{dat}_{exp}(s^{exp}_k = -1)}{2\mathcal{O}^{dat}_{exp}} - 1\right] \times (s^{exp}_k)^2,$$

where $\mathcal{O}^{dat}_{exp}(s^{exp}_k = \pm 1)$ is the experimental determination of $\mathcal{O}^{dat}_{exp}$ obtained by the variation by $\pm 1\sigma$ of the k^{th} source of uncertainty. The last term in (23) has already been discussed in Sect. 3.1.1 (11).

Notice that even though the parameters ν_{exp}, s^{exp}_k, a^ν_i, and $a^{\bar\nu}_i$ are obtained from the global χ^2 minimization, they do not enter in the counting of the degrees of freedom since they are determined by the counter-terms.

The correlated systematic uncertainties are taken into account whenever information about them is available. This is the case for H1 [12], BCDMS [64], and NMC [10]. For CDHS and BEBC, no information is available, and for E605 [13], the uncorrelated systematic uncertainties dominate. The systematic uncertainties of this later experiment are then added in quadrature and included in $\sigma^2_{dat,\rm uncor}$ of (23). As already pointed out in Sect. 3.1.3, the systematic uncertainties of the BEBC data are not known. Since these data cover the same region as the CDHS data, for both data sets we have taken into account only the statistical uncertainties (this has a negligible effect on the χ^2 minimization, since the statistical significance of these samples is rather small).

5. The MIGRAD algorithm of the MINUIT program [79] is used to minimize the χ^2.

Given the importance of nuclear effects in the treatment of the neutrino data, we performed as a check another fit, in parallel to the main fit, in which the nuclear parameters α_i of (21) are not constrained to the values $\bar{\alpha}_i$ obtained by the independent parametrization of the Fe/D structure function ratio described in Sect. 3.2.2, but are readjusted *a posteriori*. This is done by adding the coun-

[8] We thank W. van Neerven for having provided us the code computing the order-α_s Wilson coefficients published in [67].

[9] This is not the case for the latest E772 Drell–Yan data [70] and that is why we do not consider them here.

terterm

$$\sum_{i,j=1}^{3}(\alpha_i-\bar{\alpha}_i)M_{ij}^{\mathrm{Fe/D}}(\alpha_j-\bar{\alpha}_j) \tag{24}$$

to the χ^2 expression of the global pQCD analysis. In (24), $M_{ij}^{\mathrm{Fe/D}}=(1/2)\,\partial^2\chi^2_{\mathrm{Fe/D}}/\partial\alpha_i\partial\alpha_j$. We found that the two fits give very similar results.

4.3 The parametrization

Imposing the isospin symmetry leads to the following relations among the pdf: $u^{\mathrm{p}}=d^{\mathrm{n}}\equiv u$, $d^{\mathrm{p}}=u^{\mathrm{n}}\equiv d$, $\bar{u}^{\mathrm{p}}=\bar{d}^{\mathrm{n}}\equiv\bar{u}$, $\bar{d}^{\mathrm{p}}=\bar{u}^{\mathrm{n}}\equiv\bar{u}$, $s^{\mathrm{p}}=s^{\mathrm{n}}\equiv s$, $\bar{s}^{\mathrm{p}}=\bar{s}^{\mathrm{n}}\equiv\bar{s}$.

In our main fit, which we call `fit1`, the pdf $u_{\mathrm{v}}\equiv u-\bar{u}, d_{\mathrm{v}}\equiv d-\bar{d}, \bar{u}, \bar{d}, s, \bar{s}$ and g (the gluon density) are parametrized at $Q_0^2=4$ GeV^2 as follows:

$$xu_{\mathrm{v}}(x,Q_0^2)=A_{u_{\mathrm{v}}}\,x^{B_{u_{\mathrm{v}}}}\,(1-x)^{C_{u_{\mathrm{v}}}} \times(1+D_{u_{\mathrm{v}}}\,x^{E_{u_{\mathrm{v}}}}), \tag{25}$$

$$xd_{\mathrm{v}}(x,Q_0^2)=A_{d_{\mathrm{v}}}\,x^{B_{d_{\mathrm{v}}}}\,(1-x)^{C_{d_{\mathrm{v}}}} \times(1+D_{d_{\mathrm{v}}}\,x^{E_{d_{\mathrm{v}}}}), \tag{26}$$

$$x(\bar{u}+\bar{d})(x,Q_0^2)=A_+\,x^{B_+}\,(1-x)^{C_+} \times(1+D_+\,x^{E_+}), \tag{27}$$

$$x(\bar{d}-\bar{u})(x,Q_0^2)=A_-\,x^{B_-}\,(1-x)^{C_-} \times(1+D_-\,x), \tag{28}$$

$$xs(x,Q_0^2)=x\bar{s}(x,Q_0^2)=A_s\,x^{B_s}\,(1-x)^{C_s} \times(1+D_s\,x^{E_s}), \tag{29}$$

$$xg(x,Q_0^2)=A_g\,x^{B_g}\,(1-x)^{C_g} \times(1+D_g\,x^{E_g}). \tag{30}$$

This parametrization form is similar to that used in [80] (we refer to this article for a justification of this choice).

Generally it is also assumed that $s=\bar{s}$. The data samples used in the existing global analyses [19–21] cannot resolve s and $\bar{s}$ independently. In our case, the information coming from neutrino and antineutrino differential cross sections allows testing of the hypothesis $s=\bar{s}$. We thus performed another fit, called `fit2`, allowing for a charge asymmetry in the strange sea, $s\neq\bar{s}$.

Some of the parameters in (25)–(30) are determined by physical constraints. One normalization factor, say A_g, is fixed by the momentum sum rule, $\int_0^1(xg+x\sum_i(q_i+\bar{q}_i))\,\mathrm{d}x=1$. The two normalization parameters $A_{u_{\mathrm{v}}}$ and $A_{d_{\mathrm{v}}}$ are fixed by the number sum rules $\int_0^1 u_{\mathrm{v}}\mathrm{d}x=2$ and $\int_0^1 d_{\mathrm{v}}\mathrm{d}x=1$.

While the intermediate-x and large-x shape of the strange distribution is well constrained by the data entering the fit, the small-x behavior is not. Thus we set $B_s=B_+$. We also set $B_{u_{\mathrm{v}}}=B_{d_{\mathrm{v}}}=B_-$, as suggested by Regge theory. It should be noted that from a statistical point of view, these constraints do not worsen the χ^2 and are required for an invertible second derivative χ^2 matrix to be obtained.

Table 7. Contribution to the global χ^2, and number of points, of the data samples entering the fits. The values of the individual χ^2 do not include the normalization and correlated systematic shifts. The last column indicates the number of experimental parameters: overall normalization of the data sets and correlated systematics. The contributions of the experimental parameters to the χ^2 amount to 43.6 for `fit1` and 40.5 for `fit2`

Experiments	# pts.	χ^2 `fit1`	χ^2 `fit2`	# exp. param.
BCDMS (100) $\sigma^{\mu\mathrm{p}}$	94	108.0	110.8	12
BCDMS (120) $\sigma^{\mu\mathrm{p}}$	99	81.6	81.0	
BCDMS (200) $\sigma^{\mu\mathrm{p}}$	79	92.7	90.7	
BCDMS (280) $\sigma^{\mu\mathrm{p}}$	76	89.7	87.6	
BCDMS (120) $\sigma^{\mu\mathrm{D}}$	99	96.9	93.1	
BCDMS (200) $\sigma^{\mu\mathrm{D}}$	79	93.5	88.8	
BCDMS (280) $\sigma^{\mu\mathrm{D}}$	76	64.6	63.7	
BEBC $\sigma^{\nu\mathrm{p}}$	68	65.2	67.6	0
BEBC $\sigma^{\bar{\nu}\mathrm{p}}$	49	76.4	76.5	
BEBC $\sigma^{\nu\mathrm{D}}$	70	65.3	65.4	
BEBC $\sigma^{\bar{\nu}\mathrm{D}}$	49	49.7	46.7	
CDHS $\sigma^{\nu\mathrm{p}}$	45	50.6	48.6	2
CDHS $\sigma^{\bar{\nu}\mathrm{p}}$	42	53.7	53.2	
CDHSW $\sigma^{\nu\mathrm{Fe}}$	494	264.9	250.4	5
CDHSW $\sigma^{\bar{\nu}\mathrm{Fe}}$	492	274.2	277.5	
E605 (DY)	136	104.9	104.1	1
E866 A_{DY}	11	8.2	8.2	1
H1 (94-svx) F_2^{ep}	24	26.7	26.7	7
H1 (94-nvx) F_2^{ep}	156	180.6	180.3	
NMC (90) $F_2^{\mu\mathrm{p}}$	34	32.6	32.5	16
NMC (120) $F_2^{\mu\mathrm{p}}$	46	67.0	67.3	
NMC (200) $F_2^{\mu\mathrm{p}}$	61	99.4	99.3	
NMC (280) $F_2^{\mu\mathrm{p}}$	68	106.1	105.6	
NMC (90) $F_2^{\mu\mathrm{D}}$	34	24.0	23.8	
NMC (120) $F_2^{\mu\mathrm{D}}$	46	50.6	50.8	
NMC (200) $F_2^{\mu\mathrm{D}}$	61	62.6	62.7	
NMC (280) $F_2^{\mu\mathrm{D}}$	68	94.8	95.6	
NA51 A_{DY}	1	2.7	2.7	0
Total χ^2	2657	2430.8	2405.0	44

5 Results

We present now the results of our fits. The strong coupling is fixed at the value $\alpha_{\mathrm{s}}(M_{\mathrm{Z}}^2)=0.120$, which is close to the world average [81].

The contributions of the different data sample to the χ^2 are given in Table 7. The total χ^2 per degree of freedom is excellent for both fits. The amount of systematic corrections for each datum, i.e., the value of the term $[\nu_{exp}\sigma_{exp}+\sum_k\delta_k^{dat}(s_k^{exp})]$ in (23), is between -6% and +12% for all fits.

The parameters of (25)–(30) are listed in Table 8, and the parton densities are shown in Fig. 5, where they are

Table 8. Values of the parameters of the pdf at $Q_0^2 = 4$ GeV^2

	fit1	fit2
A_g	7.72	7.3
B_g	0.089	0.081
C_g	21.26	20.11
D_g	12072	6990
E_g	4.17	4.0
A_{u_v}	1.43	2.05
B_{u_v}	0.49	0.55
C_{u_v}	3.60	3.75
D_{u_v}	4.47	3.59
E_{u_v}	0.81	0.97
A_{d_v}	1.02	1.40
B_{d_v}	0.49	0.55
C_{d_v}	6.03	6.63
D_{d_v}	23.06	32.63
E_{d_v}	1.76	2.07
A_+	0.071	0.075
B_+	-0.245	-0.240
C_+	8.31	8.62
D_+	11.29	13.30
E_+	0.88	0.97
A_-	0.11	0.12
B_-	0.49	0.55
C_-	16.08	16.31
D_-	-55.62	-58.46
E_-	1	1
A_s	0.064	0.066
B_s	-0.245	-0.240
C_s	5.31	5.59
D_s	443	11354
E_s	8.26	12.04
$A_{\bar{s}}$	0.64	0.066
$B_{\bar{s}}$	-0.245	-0.240
$C_{\bar{s}}$	5.31	5.44
$D_{\bar{s}}$	443	339
$E_{\bar{s}}$	8.26	7.39

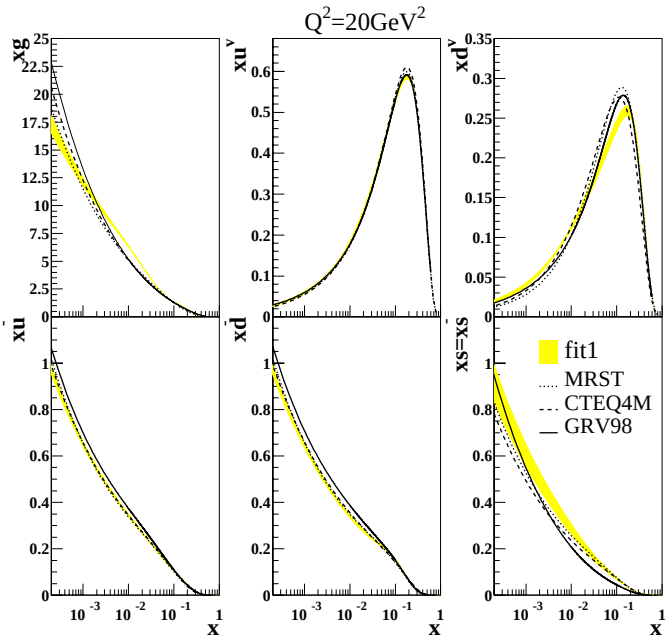

Fig. 5. The parton distribution functions of `fit1`, with their error bands, compared to the GRV98 (solid line), CTEQ4M (dashed line) and MRST (dotted line) fits. The results of `fit1` for u_v, $\bar{u}$ and $\bar{d}$ – hardly visible – nearly coincide with the MRST and CTEQ4M results

compared to the results of the other global fits. The momentum fractions of the various partons are listed in Table 9.

The parton distributions in Fig. 5 are accompanied by the error bands computed as explained in Appendix B. These do not take into account the uncertainties related to the functional choice of the pdf, nor those inherent to the treatment of the errors, which are assumed to be normally distributed. The meaning of the error bands of our pdf is the following. Once a specific form for the pdf is chosen and the constraints described in Sect. 4.3 are imposed, the error bands correspond to an increase of the χ^2 by one unit. Thus their width is determined not only by the abundance and the precision of the data, but also by the constraints on the pdf. This explains why the error bands may be small even in kinematic regions where there are no data.

With respect to the other parametrizations, our gluon density turns out to be higher at intermediate x. This could be because we do not use the prompt photon data, which tend to favor a larger glue at high x and a smaller one at intermediate x. These data are still quite controversial, and some of them seem to be in disagreement with the QCD predictions (for a recent discussion, see [82]). Also, their compatibility with the DIS data is still an unsettled issue. Our glue is determined by DIS measurements only and may be in slight disagreement with the prompt photon data at medium and high x. We will explore this problem in a future work, where we will make use of an enlarged data set.

We also find a slight discrepancy in the d_v distribution between our results and the other global fits. This is not surprising, since in our parametrization, we did not include the CDF data on the lepton asymmetry in W production at the Tevatron [83]. These data constrain the u/d ratio at $x = 0.05 - 0.1$, which is precisely the region where some difference can be seen between our $d_v(x)$ and the CTEQ and MRST distributions.

The structure function F_2 measured in different charged-lepton DIS experiments is shown in Figs. 6, 7 and 8 with the curves of `fit1`. Our fits for the Drell–Yan data are presented in Figs. 9 and 10. An excellent overall agreement is observed. In Fig. 10b we plotted the ratio $\bar{d}/\bar{u}$ at

Table 9. Fraction of the total nucleon momentum carried by the partons for three values of Q^2. The results of `fit1` (upper row) and `fit2` (lower row) are displayed. The errors are computed as explained in Appendix B

Q^2	g	u_v	d_v	$\bar{u}$	$\bar{d}$	s	$\bar{s}$
5	42.9±0.4	27.9±0.3	11.2±0.2	3.0±0.1	3.9±0.1	2.1±0.2	2.1±0.2
GeV^2	42.8±0.5	27.9±0.3	11.2±0.2	2.9±0.1	3.8±0.2	2.3±0.2	2.2±0.2
20	46.6±0.3	24.6±0.3	9.8±0.2	3.2±0.1	4.0±0.1	2.4±0.2	2.4±0.2
GeV^2	46.5±0.4	24.7±0.2	9.9±0.2	3.1±0.1	3.9±0.1	2.6±0.2	2.4±0.2
100	49.4±0.3	22.1±0.3	8.8±0.2	3.3±0.1	4.0±0.1	2.6±0.2	2.6±0.2
GeV^2	49.3±0.3	22.1±0.2	8.8±0.2	3.3±0.1	4.0±0.1	2.8±0.2	2.7±0.2

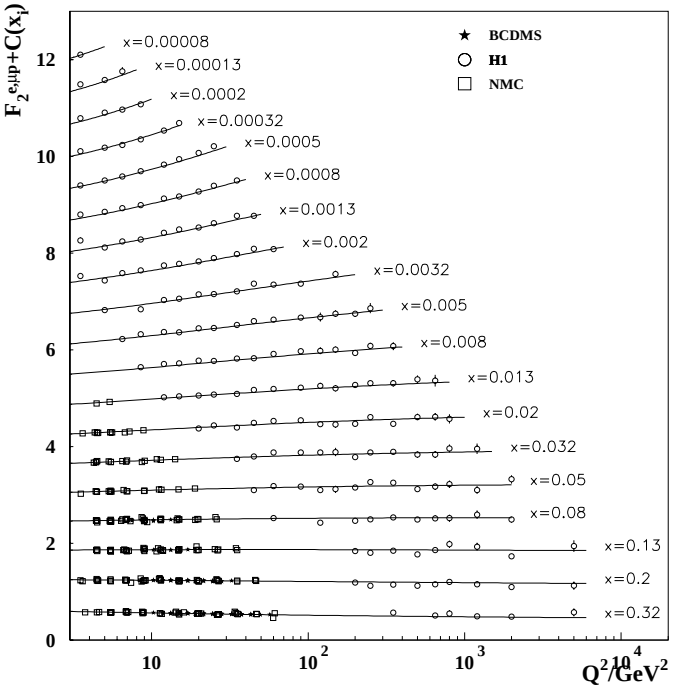

Fig. 6. H1 data vs. `fit1`. BCDMS and NMC hydrogen target data belonging to the x domain covered by H1 are also shown. These two data sets have been rebinned into the H1 x bins for plotting purposes. The data are renormalized by the overall normalization factor determined by the fit and they are plotted with an additive bin constant $c(x_i) = 0.6*(i-0.5)$ corresponding to $x_i = \{0.32, ..., 8.10^{-4}\}$. The error bars represent the quadratic sum of statistical and uncorrelated systematic errors

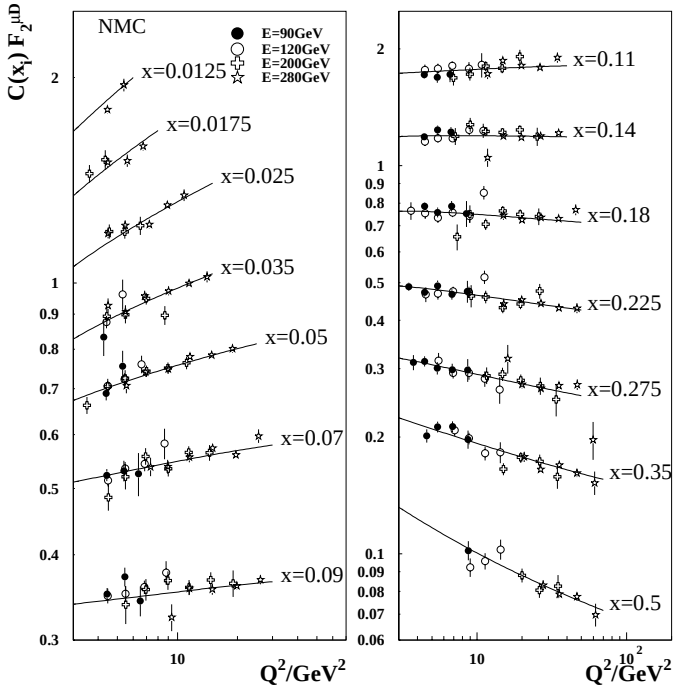

Fig. 7. NMC deuterium target data vs. `fit1`. The different beam-energy samples are shown separately. The data are renormalized by the overall normalization factor determined by the fit and multiplied by a constant $c(x_i) = \{4.8, 4, 3.2, 2.5, 2, 1.5, 1.2, 1, 7.5, 5.2, 3.7, 2.5, 1.7, 1.2, 1, 1\}$ corresponding to $x_i = \{0.0125,..., 0.07, 0.09,..., 0.5\}$. The data have been rebinned into these x_i bins for plotting purposes. The error bars represent the quadratic sum of statistical and uncorrelated systematic errors

$Q^2 = 30\text{GeV}^2$, together with its error band. Notice that the fit, which is dominated by the E866 data, yields a $\bar{d}/\bar{u}$ ratio which lies below the NA51 determination.

The reduced ν ($\bar{\nu}$) differential cross section

$$\frac{\mathrm{d}^2\sigma^r}{\mathrm{d}x\mathrm{d}y} = \frac{2\pi(M_\mathrm{W}^2+Q^2)^2}{G_\mathrm{F}^2 M_\mathrm{N} M_\mathrm{W}^4 E}\,\frac{1}{Y}\,\frac{\mathrm{d}^2\sigma}{\mathrm{d}x\mathrm{d}y}\,, \text{ with}$$
$$Y = 1+(1-y)^2 - \frac{M_\mathrm{N} x y}{E}\,, \qquad (31)$$

computed from `fit1` is compared to the data in Fig. 11 (hydrogen target), Fig. 12 (deuterium), and Fig. 13 (iron). The BEBC and CDHS hydrogen and deuterium data are well fitted down to small x. These data contribute to constraining the valence distributions without being affected by nuclear effects. Figure 13 also shows that the CDHS iron data, though they do not enter the fit, are well described by it. As for the CDHSW rejected data ($x < 0.1$), discrepancies with the fit appear only in the first bin $x = 0.045$ of Fig. 13.

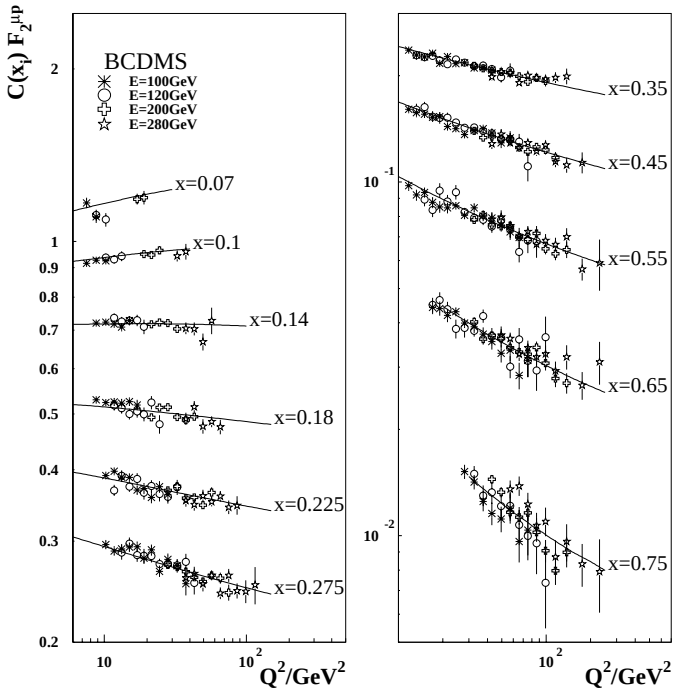

Fig. 8. BCDMS hydrogen target data compared to `fit1`. The different beam-energy samples are shown separately. The data are renormalized by the overall normalization factors, and the correlated systematic shifts determined by the fit. The error bars correspond to the quadratic sum of statistical and uncorrelated systematic errors. Because we use the BCDMS differential cross section data in our fits, the F_2 data shown in this plot have been determined by using $F_{\rm L}$ from `fit1`. The data are renormalized by the overall normalization factor determined by the fit and multiplied by a constant $c(x_i) = \{3,$ 2.5, 2, 1.5, 1.2, 1, 1, 1, 1, 1, 1$\}$ corresponding to $x_i = \{0.07,...,$ 0.275, 0.35,..., 0.75$\}$

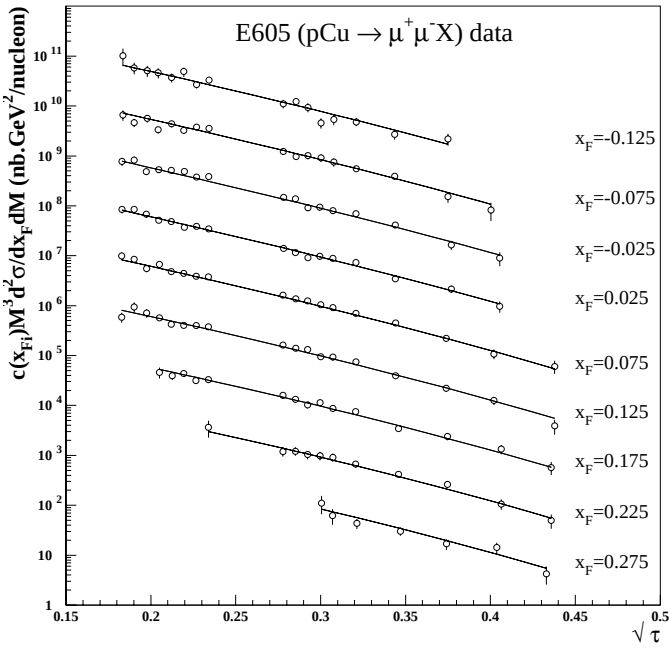

Fig. 9. E605 data vs. `fit1`. The data have been renormalized by +8%, as determined by `fit1`. The data are multiplied by a constant $c(x_{Fi}) = \{10^2, ..., 10^{10}\}$ corresponding to $x_{Fi} = \{0.275, ..., -0.125\}$. The error bars represent the quadratic sum of statistical and systematic errors

Figures 13, 8, 6, and 7 and the χ^2 results of Table 7 show explicitly that the ν and $\bar{\nu}$ iron data are compatible with the data on F_2 coming from NC charged-lepton DIS, even in the region $0.045 < x < 0.2$. By contrast, in [3,84] a sizeable discrepancy is found between the CCFR F_2^ν and the NMC F_2^μ. From the analysis performed here, which is done – we recall – on neutrino *cross sections*, no disagreement emerges between charged-lepton and neutrino DIS measurements. We checked that when the CCFR structure functions are included in our analysis, the fit worsens. We also found that the F_3 data are much better described than the F_2 data. We do not give any quantitative information about the χ^2 of this particular fit, since we considered the statistical errors only (the use of the total systematic uncertainties is not recommended by the CCFR Collaboration). In conclusion, some incompatibility seems to exist between the CCFR *structure functions* and all other charged-lepton and neutrino DIS data. A conclusive word on this matter could come from the analysis of the CCFR *cross sections*, which are unavailable at the moment.

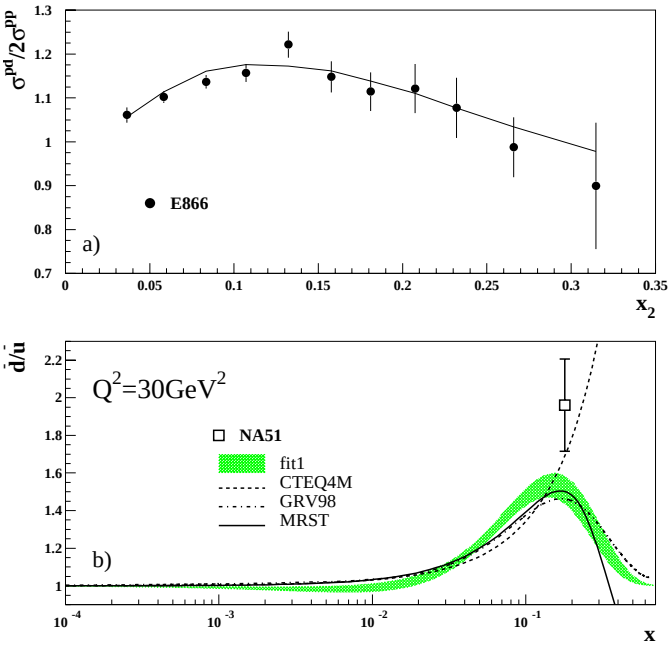

Fig. 10. a E866 vs. `fit1`. The data have been renormalized by +2% as determined in `fit1`. The error bars represent the quadratic sum of statistical and systematic errors. Notice that the data points correspond to different values of Q^2. The lines are thus an interpolation between the calculations of `fit1` **b** The NA51 result for $\bar{u}/\bar{d}$ compared to `fit1` and various parametrizations (CTEQ4M does not include the E866 data)

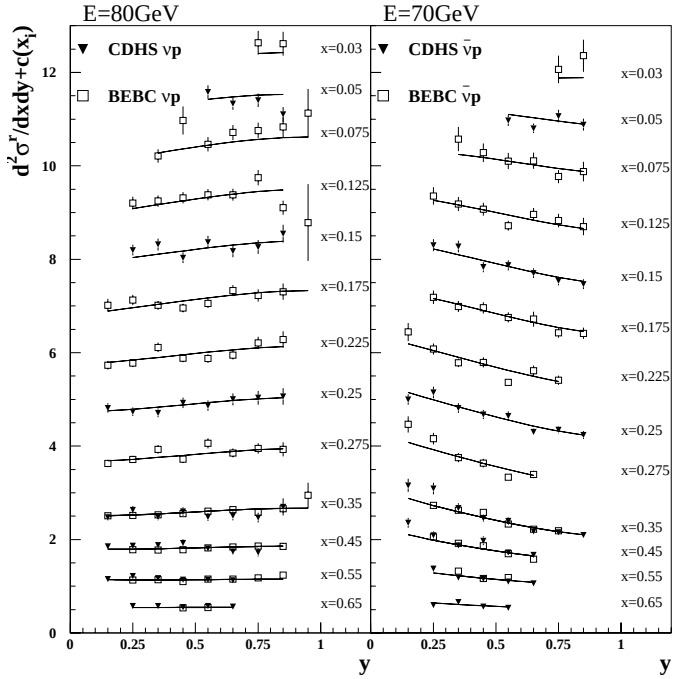

Fig. 11. CDHS and BEBC hydrogen data vs. `fit1`. The BEBC data have been rebinned into the CDHS bins for plotting purposes. The data are renormalized by the overall normalization factor determined by the fit and they are plotted with an additive bin constant $c(x_i) = \{11, 10, 9, 8, 7, 6, 5, 4, 3, 2, 1.5, 1, 0.5\}$ corresponding to $x_i = \{0.03, ..., 0.65\}$. The error bars represent the statistical errors

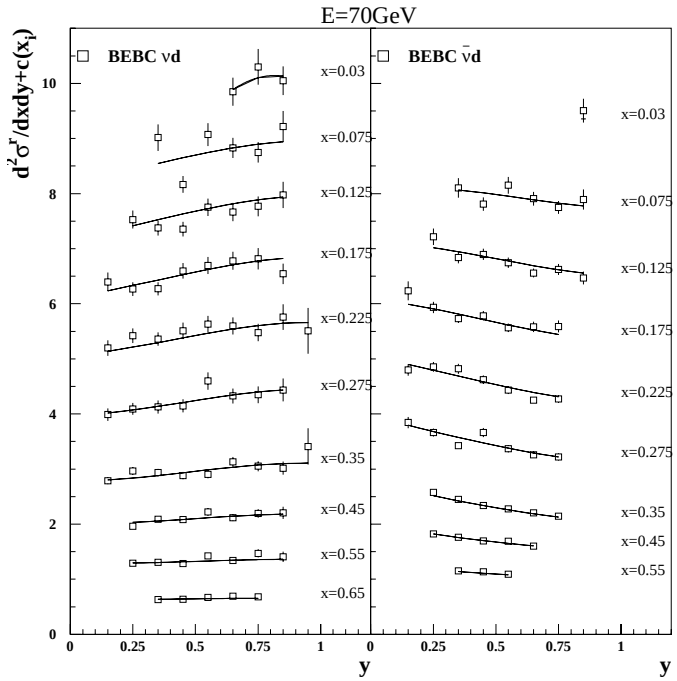

Fig. 12. Same as Fig. 11 but for the BEBC deuterium data. Here the additive bin constants are $c(x_i) = \{8.5, 7, 6, 5, 4, 3, 2, 1.5, 1, 0.5\}$

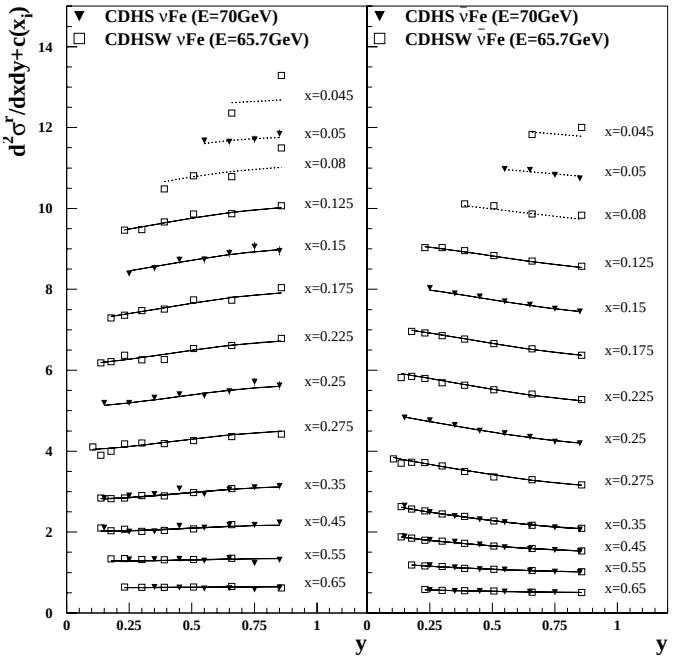

Fig. 13. Same as Fig. 11 but for the CDHSW 65.7 GeV beam data sample. The CDHS data ($E = 70$ GeV), though they do not enter the fit, are also shown. The full and dotted lines show the `fit1` results. The dotted lines describe the data rejected from `fit1` ($x < 0.1$). The nuclear correction for these particular data are taken from [3]. The error bars represent the quadratic sum of statistical and uncorrelated systematic errors. The additive bin constants are $c(x_i) = \{12, 11, 10, 9, 8, 7, 6, 5, 4, 3, 2, 1.5, 1, 0.5\}$

.

The longitudinal structure function $F_{\rm L}$ and the longitudinal-to-transverse cross section ratio R,

$$F_{\rm L} = F_2 - \left(1 + \frac{4M_{\rm N}^2 x^2}{Q^2}\right) 2xF_1 \,,$$

$$R = \frac{F_2}{2xF_1}\left(1 + \frac{4M_{\rm N}^2 x^2}{Q^2}\right) - 1,$$

computed using the pdf of `fit1` (recall that all our fits include target mass corrections) are compared to the NMC [10] and BCDMS [11] results in Fig. 14a, the H1 measurement [85] in Fig. 14b, and the CDHSW measurement [7] in Fig. 14c. Again, one can see a good agreement between our fit and the experimental results.

The beam-energy dependence of the CDHSW νFe and $\bar{\nu}$Fe data, resulting from the global χ^2 minimization, is shown in Fig. 2. The deviation from the independent linear fit of Sect. 3.1.1 is small for $\bar{\nu}$Fe data and larger for νFe.

5.1 The strange-sea density

Let us concentrate now on the strange-sea density. Because of the lack of data able to constrain it, this distribution plays a lesser role in the existing global fits. Two of

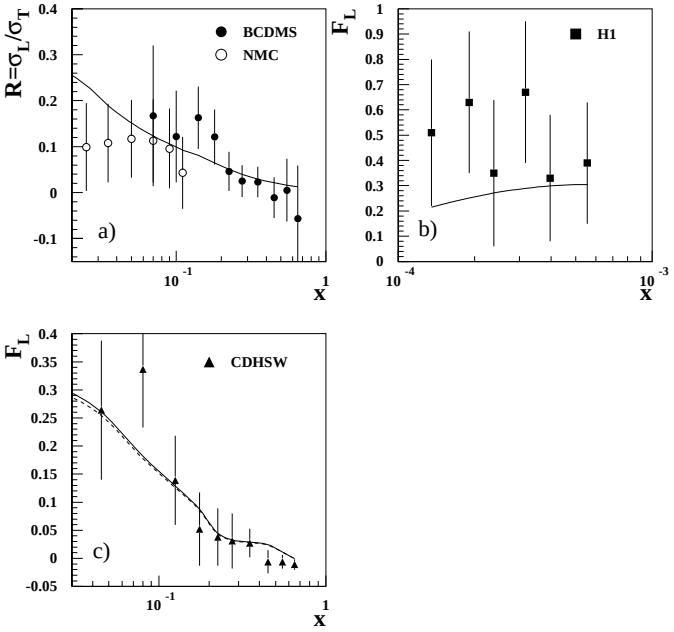

Fig. 14a–c. Results of `fit1` for the longitudinal cross sections and structure functions. Comparison of R and $F_{\rm L}$ calculated in `fit1` with: **a** the BCDMS and NMC measurements of $R = \sigma_{\rm L}/\sigma_{\rm T}$; **b** the H1 extraction of $F_{\rm L}$; **c** the CDHSW measurements (the dashed line is $F_{\rm L}^{\bar{\nu}}$; the solid line is $F_{\rm L}^{\nu}$). None of these measurements enter our fits, and only those corresponding to $Q^2 \geq 3.5\text{GeV}^2$ are shown. The error bars represent the quadratic sum of the statistical and systematic errors. Each point of these plots corresponds to different values of Q^2. The curves are obtained by smooth interpolation between the calculations performed at these points

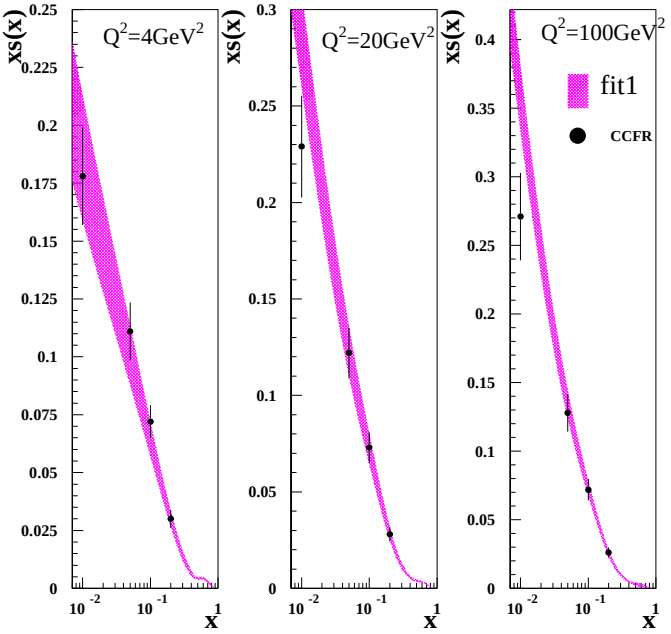

Fig. 15. The strange distribution function of `fit1`, with its error band, for three different values of Q^2. The CCFR dimuon determination (full circles with statistical and systematic errors added in quadrature) is also shown

them (CTEQ [19] and MRST [20]), guided by the results of the CCFR determination of $s(x)$ [22], in particular by the CCFR value of the strange-to-nonstrange momentum ratio $\kappa \equiv \langle x(s+\bar{s})\rangle / \langle x(\bar{u}+\bar{d})\rangle \simeq 0.5$, impose

$$s(x) + \bar{s}(x) = \frac{1}{2}\left[\bar{u}(x) + \bar{d}(x)\right] . \qquad (32)$$

In the GRV analysis [21], the strange distribution is instead set to zero at the input scale and then radiatively generated.

The abundance of our neutrino and antineutrino data sets allows us to fit $s(x)$ with no extra constraints. The resulting s distribution of `fit1` is shown, with its error band, in Fig. 5, where it is compared with the other fits. Notice that it turns out to be closer to MRST and CTEQ at large x, and to GRV at low x, where it is however much less constrained. From Table 9, one sees that in `fit1`, $\kappa = 0.67$ at $Q^2 = 20$ GeV^2.

In Fig. 15 $s(x)$ is plotted at three different Q^2 values, together with the CCFR results [22]. The agreement is good, although we must recall that the CCFR extraction of the strange distribution from dimuon production in $\nu(\bar{\nu})$Fe DIS has been criticized in many respects [18,24, 35,86].

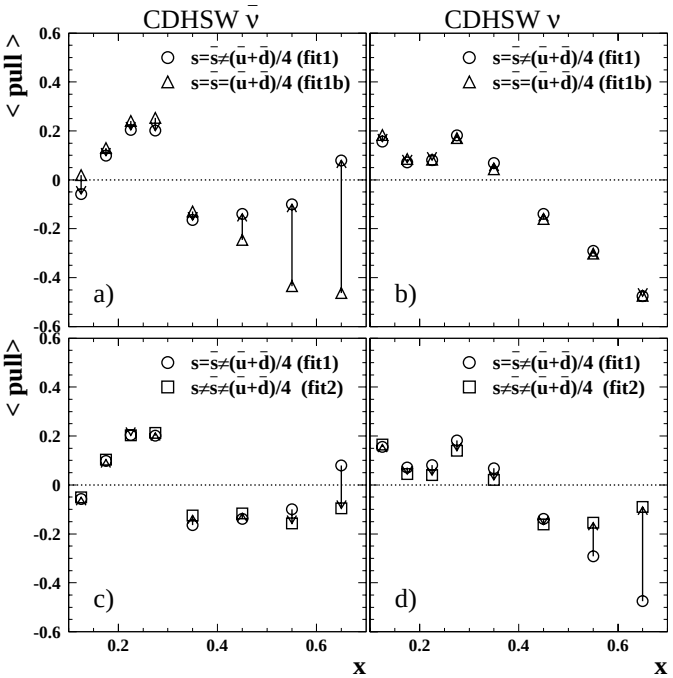

Fig. 16a–d. Mean value of the pull distribution as a function of x (see text) for CDHSW antineutrino **a** and **c** and neutrino **b** and **d** data. Three fits are compared (see text). The arrows describe the changes of the pull values when going from one fit to another

Figure 16 shows quantitatively how `fit1` is favored with respect to another fit, `fit1b`, in which the constraint (32) is imposed. The total χ^2 of `fit1b` is 2492.4, higher than the χ^2 of `fit1` by 62 units. In Fig. 16, we plotted the mean value of the so-called *pull* distribution as a function of x, for the CDHSW data:

$$\langle pull\rangle_{x_{dat}} = \frac{1}{N_{exp}(x_{dat})} \times \sum_{dat} \frac{\mathcal{O}^{dat}_{exp} - \mathcal{O}^{\rm fit}\{1-\nu_{exp}\sigma_{exp} - \sum_k \delta^{dat}_k(s^{exp}_k)\}}{\sqrt{\sigma^2_{dat,\rm stat} + \sigma^2_{dat,\rm uncor}}}, \quad (33)$$

where $N_{exp}(x_{dat})$ is the number of data at $x = x_{dat}$ for the experiment exp. In our case, exp stands for CDHSW (νFe) or CDHSW ($\bar\nu$Fe). One can see from Figs. 16a and 16b that it is the $\bar\nu$ data which tend to favor `fit1` with respect to `fit1b`.

A very interesting question is whether the strange distribution is equal or not to the antistrange one. The usual assumption $s(x) = \bar s(x)$ is not in fact dictated by first principles.

We thus looked for a possible charge asymmetry of the strange sea by performing a fit, called `fit2`, in which we release the constraint $s = \bar s$. From Table 5, one can see that the attempt to disentangle the s and $\bar s$ distributions is justified by the abundance of antineutrino events in our data set.

The parametrization (29) for $s = \bar s$ is replaced in `fit2` by two independent functions for s and $\bar s$,

$$xs(x,Q^2_0) = A_s\, x^{B_s}\,(1-x)^{C_s}\,(1+D_s\,x^{E_s}), \quad (34)$$

$$x\bar s(x,Q^2_0) = A_{\bar s}\, x^{B_{\bar s}}\,(1-x)^{C_{\bar s}}\,(1+D_{\bar s}\,x^{E_{\bar s}}). \quad (35)$$

We set $A_{\rm s} = A_{\bar s}$ and $B_{\rm s} = B_{\bar s}$, and we fix one more parameter by imposing $\int_0^1 (s-\bar s)\,{\rm d}x = 0$ (no net strangeness).

The main results of `fit2` are:

- The minimum χ^2 decreases by 25 units with respect to `fit1` (see Table 7). Hence the choice $s \neq \bar s$ is slightly favored.
- The strange distribution turns out to be harder than the antistrange one. The difference $s - \bar s$ is shown in Fig. 17a with its error band. In Fig. 17b, we plot the ratio $s/\bar s$ at $Q^2 = 20$ GeV^2.
- The momentum fractions of the `fit2` partons at different Q^2 values are listed in Table 9. The momentum fraction $\langle xs\rangle$ is larger than $\langle x\bar s\rangle$. Notice also that `fit2` favors a higher value for the strange-to-nonstrange momentum ratio κ, with respect to the fit with $s = \bar s$.

Let us comment now on a previous test of the strange-sea asymmetry. In [22], the CCFR Collaboration found no evidence for $s \neq \bar s$. In their analysis, the constraint $s(x) = [\bar u(x) + \bar d(x)] \times A(1-x)^C$ was imposed; this limits the flexibility of the fit. Moreover, the dimuon sample of CCFR does not cover the high-x region and consists only of 5000 neutrino events and 1000 antineutrino events. Our analysis does not have these limitations (our data sample is much more balanced between neutrino and antineutrino events, and no extra constraints are set but those ensuring

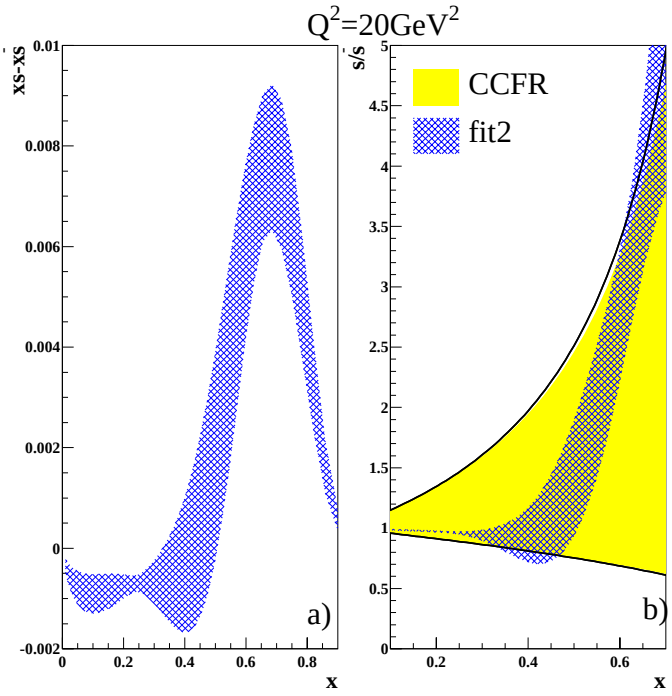

Fig. 17a,b. Results of `fit2` for: **a** the difference $x(s-\bar s)$ and **b** the ratio $s/\bar s$ at $Q^2 = 20{\rm GeV}^2$. In the box **b**, the result of CCFR is also shown

no net strangeness), and it gives a more precise result on $s/\bar s$, as one can see from Fig. 17.

In order to understand how the difference $s - \bar s$ is constrained by the data, let us consider the quantity

$$\Delta^{\nu-\bar\nu} \equiv \frac{4\pi x(M^2_{\rm W}+Q^2)^2}{G^2_{\rm F}M^4_{\rm W}}\left[\frac{{\rm d}^2\sigma^{\nu{\rm N}}}{{\rm d}x{\rm d}Q^2} - \frac{{\rm d}^2\sigma^{\bar\nu{\rm N}}}{{\rm d}x{\rm d}Q^2}\right]. \quad (36)$$

The flavor content of $\Delta^{\nu-\bar\nu}$ is more evident in the parton model, where it reads

$$\Delta^{\nu-\bar\nu} \propto xs(x) - x\bar s(x) + Y_-[xu_{\rm v}(x) + xd_{\rm v}(x)], \quad (37)$$

with $Y_- = 1-(1-y)^2$. The $\nu - \bar\nu$ cross section difference (36) is plotted as a function of Y_-, at fixed x and Q^2, in Fig. 18. Comparing `fit1` and `fit2`, one can see that their results deviate with increasing x (being very close to each other for $x \lesssim 0.3$). At high-x, `fit1` undershoots the CDHSW values of Δ^ν for all Q^2 bins. Fig. 18 shows that the CDHSW data are more precise at high-y. Hence it is this region which drives the result on $s - \bar s$. Looking at Fig. 16c,d, one sees also that it is the ν data which favor `fit2` with respect to `fit1`.

Since the nuclear corrections applied to the CDHSW data are sizeable (see Fig. 4b), one may naturally ask to what extent our results are affected by the uncertainties regarding the evaluation of these corrections. The Fe/D ratio, as we have seen (see Fig. 3 and the check described at the end of Sect. 4.2), is well determined by the charged-lepton data. Moreover, it factorizes in the $\nu - \bar\nu$ difference. Hence this component of the nuclear correction

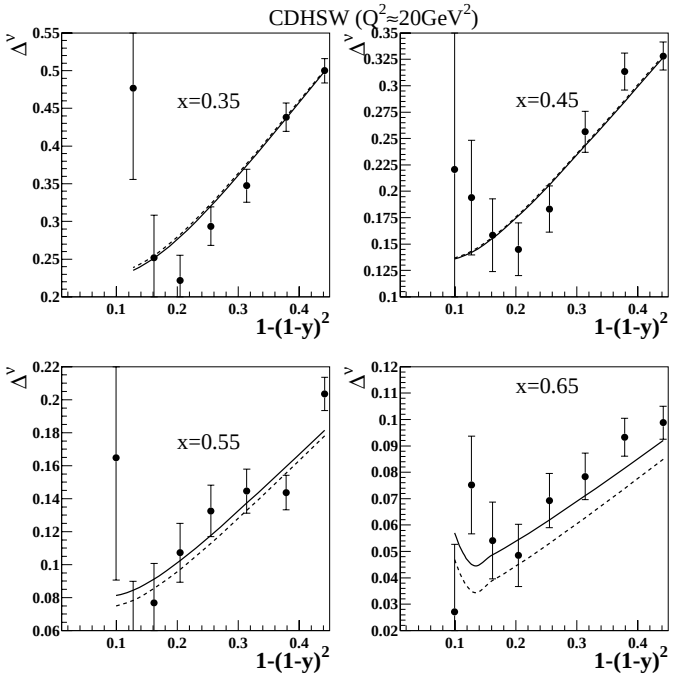

Fig. 18. Difference between the νFe and $\bar{\nu}$Fe CDHSW differential cross sections (see (36)) at fixed x and $Q^2 \approx 20$ GeV^2 as a function of $Y_- = 1-(1-y)^2$. The solid line corresponds to `fit2`, the dashed line to `fit1`. The exact values of Q^2 are 22, 21.6, 20.3, and 18.6 GeV^2 for $x = 0.35$, 0.45, 0.55, *and*0.65, respectively

is rather harmless. The isoscalarity corrections are, however, different for neutrino and antineutrino observables and are quite large. Looking at (17, 20), one sees that the isoscalarity ratio cannot exceed $A/(2Z) = 1.073$ for iron. Fig. 4a shows that the maximal value we obtained is not far from this upper bound. We found that when the isoscalarity ratio is reduced, the resulting $s - \bar{s}$ difference gets larger. Thus we conclude that our results on the strange-sea asymmetry are not spoiled, at least qualitatively, by the uncertainties on the isoscalarity corrections.

Theoretically, a charge-asymmetric sea is accounted for by introducing a distinction between extrinsic and intrinsic $q\bar{q}$ pairs [87]. The extrinsic sea consists of short-lived quarks and antiquarks produced by QCD hard subprocesses (bremsstrahlung and gluon splitting). It is evident that the extrinsic component of the sea cannot be charge asymmetric. On the other hand, the intrinsic $q\bar{q}$ pairs exist over a longer time scale and are associated with nonperturbative phenomena. These pairs are still produced by gluon fragmentation but have time, before recombining, to interact with other partons. They represent higher Fock states of the nucleon ($|qqqq\bar{q}\ldots\rangle$) and manifest themselves in meson–baryon fluctuations.

There is no fundamental principle forbidding a possible charge asymmetry of the intrinsic sea. Actually, there are reasons to believe that such asymmetry should indeed be a property of the strange and charmed sea [87–89]. If the strange (or charmed) sea is asymmetric at low Q^2 because of some nonperturbative mechanism, the QCD evolution simply preserves this asymmetry because $s - \bar{s}$ (or $c - \bar{c}$) evolves like a nonsinglet distribution, and its first moment is constant. An interesting feature of the intrinsic sea is that it tends to exist at relatively large values of x [87–89], corresponding to the most energetically favored configuration of the nucleon light–cone wave function.

In the simplest model [90,88,89], the production of the intrinsic strange sea is attributed to the $p \to \Lambda K^+$ fluctuation. Due to chiral symmetry pseudoscalar mesons have relatively small masses. As a consequence [88], the average x of the $\bar{s}$ antiquark in the K is smaller that the average x of the s quark coming from the Λ. Thus the s distribution is expected, on quite general grounds, to be harder than the $\bar{s}$ distribution. This expectation has been substantiated by explicit calculations in [90,89,91] (for other models, see [92]). Our results on the strange- and antistrange-sea density are, at least qualitatively, in agreement with the predictions of the intrinsic sea theory.

6 Conclusions

We have presented a global next-to-leading- order QCD analysis of a large set of DIS data, including the (properly reevaluated) neutrino and antineutrino differential cross sections of BEBC, CDHS, and CDHSW, the charged-lepton structure functions of NMC, BCDMS, and H1, and the Drell–Yan data of E605, NA51, and E866. The full use of the information on the nucleon structure embodied in neutrino DIS observables and a proper treatment of the experimental systematic uncertainties are the main novelties of our approach. In particular, the large-statistics CDHSW iron data allow disentanglement of the strange sector from the nonstrange one; this leads to a consistent determination of $s(x)$ within a global fit similar to what happens for the other parton distributions.

The charm mass effects, whose relevance for an accurate determination of the parton densities is a recent firm acquisition, have been consistently treated in a massive factorization scheme, the fixed flavor scheme.

We found no evidence of any discrepancy between the neutrino data we considered in our fit and the charged-lepton data. A complete and unambiguous analysis of *all* neutrino experiments and a conclusive check of the compatibility of their data with the charged-lepton data would be possible only if we could use the CCFR differential cross sections, which are unfortunately not available.

The large statistics of antineutrino events in our data sample allowed us to test the hypothesis of a charge-asymmetric strange sea: $s \neq \bar{s}$. We found some evidence for such an asymmetry. The qualitative features of the resulting s and $\bar{s}$ distributions (namely, a large x tail at low Q^2 and $\bar{s}(x)$ softer than $s(x)$) agree with the expectations of the intrinsic sea theory.

Finally, we outline some developments. As for the strong coupling, in the present work we took a pragmatic attitude, using the world average value. A more systematic study, in which we will extract α_s from the DIS data

and investigate its correlation with the gluon density, will be presented in a forthcoming paper.

Another important development that we have in mind is the comparison of the results obtained in the two QCD massive schemes, FFS and VFS.

Finally, one should envisage some independent, and perhaps more direct, experimental test of the charge asymmetry of the strange sea, for which we presented here only indirect statistical evidence.

Acknowledgements. We thank J. Blümlein, V. Del Duca, S. Forte, G. Korchemski, M.W. Krasny, B.-Q. Ma, V. Massoud, W. Melnitchouk, A. Milsztajn, N.N. Nikolaev, and W. Seligman for valuable help and/or useful discussions. Two of us (C.P. and F.Z.) would like to thank their H1 colleagues for their help in elaborating the pQCD analysis program.

Appendix A: Unfolding procedure

A two-dimension net in x and y is defined. The nodes correspond to the centers of the experimental bins. Following [77], we define a basis of continuous functions $\phi_i(x)$ and $\psi_j(y)$ such that $\phi_i(x_l^{\rm c}) = \delta_{il}$ and $\psi_j(y_m^{\rm c}) = \delta_{jm}$ (where δ_{il} is the Kronecker symbol). Provided these functions are determined using a spline interpolation [93], the differential cross section can be written as

$$\frac{{\rm d}^2\sigma^{\nu(\bar{\nu})\rm Fe}(x,y,E_k^{\rm c})}{{\rm d}x{\rm d}y} = \sum_{l=1}^{n_x}\sum_{m=1}^{n_y}\phi_i(x)\psi_j(y) \times \frac{{\rm d}^2\sigma^{\nu(\bar{\nu})\rm Fe}(x_l^{\rm c},y_m^{\rm c},E_k^{\rm c})}{{\rm d}x{\rm d}y}. \quad (38)$$

Applying the average theorem, we derive from (38)

$$\sigma_{ijk} = \sum_{l=1}^{n_x}\sum_{m=1}^{n_y} c_x^{i,{\rm l}} c_y^{j,m} \frac{{\rm d}^2\sigma^{\nu(\bar{\nu})\rm Fe}(x_l^{\rm c},y_m^{\rm c},E_k^{\rm c})}{{\rm d}x{\rm d}y} \quad (39)$$

with

$$\sigma_{ijk} \approx \frac{N_{ijk}}{C}, \quad c_x^{i,{\rm l}} = \frac{\int_{x_i}^{x_{i+1}}\phi_l(x){\rm d}x}{x_{i+1}-x_i},$$
$$c_y^{j,m} = \frac{\int_{y_j}^{y_{j+1}}\psi_m(y){\rm d}y}{y_{j+1}-y_j}$$

where N_{ijk} is the number of events experimentally observed and C is the number of scattering centers in the target.

The differential cross sections at the bin centers ${\rm d}^2\sigma^{\nu(\bar{\nu})\rm Fe}(x_l^{\rm c},y_m^{\rm c},E_k^{\rm c})/{\rm d}x{\rm d}y$ are obtained by the reversal of this system of $n_x \times n_y$ equations. Numerically, the more stable results were obtained by the use of the first-order spline. In this case, $\phi_i(x)$ and $\psi_j(y)$ are the Lagrangian (or "hat") functions [93]

$$\phi_i(x) = \begin{cases} (x-x_{i-1})/(x_i-x_{i-1}), & x_{i-1} \le x \le x_i \\ (x_{i+1}-x)/(x_{i+1}-x_i), & x_i \le x \le x_{i+1} \\ 0 & \text{otherwise.} \end{cases} \quad (40)$$

The same expression holds for $\psi_j(y)$.

However, using (40), one can see that the system of (39) is incomplete if $x_1 \neq 0$ or $x_{n_x} \neq 1$ or $y_1 \neq 0$ or $y_{n_y} \neq 1$. Indeed, the boundary bins receive some contributions (in the r.h.s. of (39)) coming from the bin neighbors that are not included in the measurements. To overcome this difficulty, we have defined artificial extra bins $[x_{n_x}, x_{n_x+1}]$ $\forall y$, $[y_0, y_1]$ $\forall x$ and $[y_{n_y}, y_{n_y+1}]$ $\forall x$. Then we fixed the cross section at the center of these new bins to a certain fraction λ of the closest cross section measurement. Under this modification, (39) becomes an inhomogeneous system,

$$\sigma_{i,j,k} - \lambda\Bigg(c_x^{i,n_x+1}c_y^{j,0}\sigma_{n_x,1,k} + c_x^{i,n_x+1}c_y^{j,n_y+1}\sigma_{n_x,n_y,k} + \sum_{m=1}^{n_y} c_x^{i,n_x+1}c_y^{j,m}\sigma_{n_x,j,k} + \sum_{l=1}^{n_x} c_x^{i,{\rm l}}[c_y^{j,0}\sigma_{l,1,k} + c_y^{j,n_y+1}\sigma_{l,n_y,k}]\Bigg) = \sum_{l=1}^{n_x}\sum_{m=1}^{n_y} c_x^{i,{\rm l}}c_y^{j,m}\frac{{\rm d}^2\sigma^{\nu(\bar{\nu})\rm Fe}(x_l^{\rm c},y_m^{\rm c},E_k^{\rm c})}{{\rm d}x{\rm d}y}, \quad (41)$$

and the differential cross sections at the bin centers are obtained by the inversion of this system with $\lambda = 1$.

In order to test the sensitivity of our results to the choice of λ, we have set λ to some extreme values: $\lambda = 2$, $\lambda = 1/2$. We observed a variation of the order of $\approx 20\%$ in the highest x bin for all y bins. But we point out that the results are completely stable in the first $x < 0.1$ bins for all y bins. This method is then used to perform the definitive bin center correction in these particular bins, as mentioned in Sect. 3.1.1. We estimate the uncertainty of the method by repeating the procedure using a second-order spline interpolation to define the basis functions $\phi_i(x)$ and $\psi_j(y)$. The ratio of the two bin center correction factors is then taken, bin by bin, as an estimate of the uncertainty due to the method, and added in quadrature to the uncorrelated systematic error of the measurement (it is of the order of $\lesssim 2\%$ and reaches 7.5% at high y).

Appendix B: Error bands

We describe here the formula used to calculate the error bands shown throughout the paper. If we call $\mathbf{p} \equiv \{p_1, ..., p_n\}$ the vector of the free parameters of the fit, the error band of a given function f is given at each (x, Q^2) point by [94]:

$$\Delta f(x,Q^2;\boldsymbol{p}_0) = |f(x,Q^2;\boldsymbol{p}_0 + \boldsymbol{\Delta}_p(x,Q^2)) - f(x,Q^2;\boldsymbol{p}_0 - \boldsymbol{\Delta}_p(x,Q^2))| \quad (42)$$

where $\boldsymbol{p}_0$ denotes the parameter set minimizing the χ^2, and the vector $\boldsymbol{\Delta}_p(x,Q^2) \equiv \{\Delta_{p_1}(x,Q^2), ..., \Delta_{p_n}(x,Q^2)\}$ is given by

$$\boldsymbol{\Delta}_p(x,Q^2) = \frac{M^{-1}\boldsymbol{\partial}_p f(x,Q^2;\boldsymbol{p})}{\sqrt{\boldsymbol{\partial}_p f(x,Q^2;\boldsymbol{p}) M^{-1} \boldsymbol{\partial}_p f(x,Q^2;\boldsymbol{p})}} \quad (43)$$

with $M_{ij} = (1/2)\,\partial^2\chi^2/\partial p_i \partial p_j$ and $\boldsymbol{\partial}_p = \{\partial/\partial p_1, ..., \partial/\partial p_n\}$.

References

1. See for instance: M. Diemoz, F. Ferroni, E. Longo, Phys. Rep. **130**, 293 (1986); T. Sloan, G. Smadja, R. Voss, Phys. Rep. **162**, 45 (1988); J.M. Conrad, M.H. Shaevitz, T. Bolton, Rev. Mod. Phys **70**, 1341 (1998); A.M. Cooper-Sarkar, R.C. Devenish, A. De Roeck, Int. J. Mod. Phys. A **13**, 3385 (1998)
2. See for instance, J.F. Owens, W.K. Tung, Annu. Rev. Nucl. Part. Sci. **42**, 291 (1992)
3. W.G. Seligman, Ph.D. Thesis, Columbia University, Nevis Report-292, 1997
4. W.K. Krasny, Habilitation Thesis, I.N.P Cracow, TPJU-22/89, 1989
5. G.T. Jones, et al., Z. Phys. C **62**, 575 (1994) and references therein
6. H. Abramowicz, et al., CDHS Collaboration, Z. Phys. C **25**, 29 (1984)
7. P. Berge, et al., CDHSW Collaboration, Z. Phys. C **49**, 187 (1991)
8. F. Bergsma, et al., CHARM Collaboration, Phys. Lett. B **123**, 269 (1983)
9. W.C. Leung, et al., CCFR Collaboration, Phys. Lett. B **317**, 655 (1993); P.Z. Quintas, et al., CCFR Collaboration, Phys. Rev. Lett. **71**, 1307 (1993)
10. M. Arneodo, et al., NMC Collaboration, Nucl. Phys. B **483**, 3 (1997)
11. A.C. Benvenuti, et al., BCDMS Collaboration, Phys. Lett. B **223**, 485 (1989); Phys. Lett. B **237**, 592 (1989)
12. H1 Collaboration, Nucl. Phys. B **470**, 3 (1996)
13. G. Moreno, et al., E605 Collaboration, Phys. Rev. D **43**, 2815 (1991)
14. A. Baldit, et al., NA51 Collaboration, Phys. Lett. B **332**, 244 (1994)
15. E.A. Hawker at al., E866 Collaboration, Phys. Rev. Lett. **80**, 3715 (1998)
16. A. Milsztajn, et al., Z. Phys. C **49**, 527 (1991)
17. M. Gluck, E. Reya, M. Stratmann, Nucl. Phys. B **422**, 37 (1994)
18. V. Barone, et al., Phys. Lett. B **328**, 143 (1991); Phys. Lett. B **317**, 433 (1993); Z. Phys. C **70**, 83 (1996)
19. H.L. Lai, et al., CTEQ Collaboration, Phys. Rev. D **55**, 1280 (1997)
20. A.D. Martin, R.G. Roberts, W.J. Stirling, R.S. Thorne, Eur. Phys. J. C **4**, 463 (1998)
21. M. Glück, E. Reya, A. Vogt, Eur. Phys. J. C **5**, 461 (1998)
22. A.O. Bazarko, et al., CCFR Collaboration, Z. Phys. C **65**, 189 (1995); A.O. Bazarko, Ph.D. Thesis, Columbia University, Nevis report 285
23. M.A.G. Aivazis, et al., Phys. Rev. D **50**, 3102 (1994)
24. V. Barone, M. Genovese, Phys. Lett. B **379**, 233 (1996)
25. V. Barone, U. D'Alesio, M. Genovese, in Proceedings of the Workshop on Future Physics at HERA, edited by G. Ingelman, A. De Roeck, R. Klanner, (DESY 1996), p. 102
26. W.J. Marciano, Phys. Rev. D **29**, 580 (1984)
27. E. Witten, Nucl. Phys. B **104**, 445 (1976); M. Glück, E. Reya, Phys. Lett. B **83**, 98 (1979)
28. W. Furmanski, R. Petronzio, Z. Phys. C **11**, 293 (1982)
29. W.L. van Neerven, E.B. Zijlstra, Phys. Lett. B **272**, 127 (1991); Phys. Lett. B **273**, 476 (1991); Nucl. Phys. B **383**, 525 (1992)
30. V.N. Gribov, L.N. Lipatov, Sov. J. Nucl. Phys. **15**, 438 (1972); G. Altarelli, G. Parisi, Nucl. Phys. B **126**, 298 (1977); Yu.L. Dokshitzer, Sov. Phys. JETP **46**, 641 (1977)
31. E. Laenen, et al., Nucl. Phys. B **392**, 162, 229 (1993); Phys. Lett. B **291**, 325 (1992)
32. S. Riemersma, J. Smith, W.L. van Neerven, Phys. Lett. B **347**, 143 (1995)
33. T. Gottschalk, Phys. Rev. D **23**, 56 (1981)
34. U. D'Alesio, Ph.D. Thesis, Torino University, 1996
35. M. Glück, S. Kretzer, E. Reya, Phys. Lett. B **380**, 171 (1996); (erratum); ibid., B **405**, 391 (1997)
36. A. De Rùjula, R. Petronzio, Nucl. Phys. B **154**, 394 (1979)
37. D.Y. Bardin, O.M. Fedorenko, Yad. Phys. **30**, 811 (1979)
38. D.Y. Bardin, V.A. Dokuchaeva, preprint JINR-E2-86-260 (1986)
39. J. Blümlein, Z. Phys. C **65**, 293 (1995)
40. A. Arbuzov, et al., HECTOR program version 1.00, DESY 95-185
41. L.W. Whitlow, et al., Phys. Lett. B **282**, 475 (1992); L.W. Whitlow, Ph.D. Thesis, SLAC-Report-357, 1990
42. A.J. Buras, K.J.F. Gaemers, Nucl. Phys. B **132**, 249 (1978)
43. P. Berge, et al., CDHSW Collaboration, Z. Phys. C **35**, 443 (1987)
44. B. Vallage, Ph.D. Thesis, Université Paris 11, 1986 (in French)
45. S.A. Rabinowitz, et al., CCFR Collaboration, Phys. Rev. Lett. **70**, 134 (1993)
46. P.H. Slander, et al., CCFR Collaboration, Phys. Rev. D **42**, 759 (1990)
47. M. Aderholz, et al., WA21 Collaboration, Phys. Lett. B **173**, 211 (1986)
48. U.F. Katz, Ph.D. Thesis, Max-Planck-Institut für Physik, München, MPI-PhE/92-03, 1992 (in German)
49. V. Barone, E. Predazzi, Ann. Phys. Fr. **12**, 525 (1987); D.F. Geesaman, K. Saito, A.W. Thomas, et al., Annu. Rev. Nucl. Part. Sci. **45**, 337 (1995)
50. M. Arneodo, Phys. Rep. **240**, 301 (1994)
51. W. Melnitchouk, A.W. Schreiber, A.W. Thomas, Phys. Lett. B **335**, 11 (1994)
52. V. Barone, et al., Phys. Lett. B **321**, 137 (1994); B. Badełek, J. Kwieciński, Phys. Rev. D **50**, 4 (1994)
53. A. Amaudruz, NMC Collaboration, Nucl. Phys. B **441**, 3 (1995); M. Arneodo, et al., NMC Collaboration, Nucl. Phys. B **441**, 12 (1995)
54. J. Kwieciński, B. Badełek, Phys. Lett. B **208**, 508 (1988)
55. W. Melnitchouk, A.W. Thomas, Phys. Rev. C **52**, 3373 (1995)
56. N.N. Nikolaev, V.I. Zakharov, Phys. Lett. **55B**, 397 (1975); N.N. Nikolaev, B.G. Zakharov, Z. Phys. C **49**, 607 (1991)
57. V. Barone, et al., Z. Phys. C **58**, 541 (1993)
58. M.R. Adams, et al., E665 Collaboration, Z. Phys. C **67**, 403 (1995)
59. P.P. Allport, et al., WA59 Collaboration, Phys. Lett. B **232**, 417 (1989)
60. B.Z. Kopeliovich, P. Marage, Int. J. Mod. Phys. A **8**, 1513 (1993)

61. R. Kobayashi, S. Kumano, M. Miyama, Phys. Lett. B **354**, 465 (1995)
62. J. Gomez, et al., E139 Collaboration, Phys. Rev. D **49**, 4348 (1994)
63. A.C. Benvenuti, et al., BCDMS Collaboration, Phys. Lett. B **189**, 483 (1987)
64. A.C. Benvenuti, et al., BCDMS Collaboration, CERN-EP/89-06; CERN-EP/89-170
65. M. Derrick, et al., ZEUS Collaboration, Z. Phys. C **72**, 399 (1996)
66. F. Lehner, Ph.D. Thesis, University of Hamburg, 1998 (in German)
67. P.J. Rijken, W.L. van Neerven, Phys. Rev. D **51**, 44 (1995)
68. P.J. Rijken, W.L. van Neerven, Phys. Rev. D **52**, 149 (1995)
69. M. Dasgupta, B.R. Webber, Phys. Lett. B **382**, 273 (1996); Y.L. Dokshitzer, et al., Nucl. Phys. B **469**, 93 (1996)
70. P.L. McGaughey, et al., E772 Collaboration, Phys. Rev. D **50**, 3038 (1994)
71. M. Virchaux, A. Milsztajn, Phys. Lett. B **274**, 221 (1992)
72. H. Georgi, H.D. Politzer, Phys. Rev. D **14**, 1829 (1976); R. Barbieri, et al., Nucl. Phys. B **117**, 50 (1976)
73. M.R. Adams, et al., E665 Collaboration, Phys. Rev. D **54**, 3006 (1996)
74. C. Adloff, et al., H1 Collaboration, Nucl. Phys. B **497**, 3 (1997)
75. J. Breitweg, et al., ZEUS Collaboration, Phys. Lett. B **407**, 432 (1997)
76. U.K. Yang, et al., CCFR Collaboration, J. Phys. G **22**, 775 (1996)
77. C. Pascaud, F. Zomer, DESY preprint DESY/96-266
78. J. Blümlein, et al., in Proceedings of the Workshop on Future Physics at HERA, edited by G. Ingelman, A. De Roeck, R. Klanner (DESY 1996), p. 23
79. CERN Program Library Long Writeup D506, CERN 1993
80. H.L. Lai, et al., CTEQ Collaboration, Phys. Rev. D **51**, 4763 (1995)
81. Particle Data Group, Review of Particle Properties, Eur. Phys. J. C **3**, 1 (1998)
82. P. Aurenche, et al., Eur. Phys. J. C **9**, 107 (1999)
83. F. Abe, et al., CDF Collaboration, Phys. Rev. Lett. **74**, 850 (1995)
84. W.G. Seligman, et al., CCFR Collaboration, Phys. Rev. Lett. **79**, 1213 (1997)
85. C. Adloff, et al., H1 Collaboration, Phys. Lett. B **393**, 452 (1997)
86. M. Glück, S. Kretzer, E. Reya, Phys. Lett. B **398**, 381 (1997); (E) ibid. B **405**, 392 (1997)
87. S.J. Brodsky, P. Hoyer, C. Peterson, N. Sakai, Phys. Lett. B **93**, 451 (1980); S.J. Brodsky, C. Peterson, N. Sakai, Phys. Rev. D **23**, 2745 (1981)
88. M. Burkardt, B.J. Warr, Phys. Rev. D **45**, 958 (1992)
89. S.J. Brodsky, B.-Q. Ma, Phys. Lett. B **381**, 317 (1996)
90. A.I. Signal, A.W. Thomas, Phys. Lett. B **191**, 205 (1987)
91. H. Holtmann, A. Szczurek, J. Speth, Nucl. Phys. A **596**, 631 (1996); A. Szczurek, A.J. Buchmann, A. Faessler, J. Phys. G **22**, 1741 (1996)
92. X. Ji, J. Tang, Phys. Lett. B **362**, 182 (1995); W. Melnitchouk, M. Malheiro, hep-ph/9901321
93. C. de Boor, A Practical Guide to Spline (Springer, New York 1978)
94. C. Pascaud, F. Zomer, LAL preprint LAL/95-05